A Study of Seismoelectric Signals in Measurement While Drilling

By

Xin Zhan

B.E. Photographic Surveying and Remote Sensing
Wuhan University, 2002

Submitted to the Department of Earth, Atmospheric and Planetary Sciences in

Partial Fulfillment of the Requirements for the Degree of

Master of Science in Earth and Planetary Sciences

at the

© Massachusetts Institute of Technology

September 2005

Signature of Author: _____

Department of Earth, Atmospheric and Planetary Sciences
Sep 9, 2005

Certified by: _____

M. Nafi Toksöz
Professor of Geophysics
Thesis Supervisor

Accepted by: _____

Maria T. Zuber
E.A. Griswold Professor of Geophysics and Planetary Science
Department Head

A Study of Seismoelectric Signals in

Measurement While Drilling

By

Xin Zhan

Submitted to the Department of Earth, Atmospheric and Planetary Sciences

on Sep 9, 2005 in partial fulfillment of the requirements for the degree of

Master of Science in Earth and Planetary Sciences

Abstract

An LWD acoustic wave can move the excess charge in the electric double layer along the borehole wall to generate a streaming electric field. This thesis is an experimental and theoretical investigation of the electric field induced by the multipole LWD acoustic wave. The main goal of this thesis is to understand the mechanism in the seismoelectric conversion under the LWD geometry and prove the absence of the tool mode in the LWD-acoustic-wave induced electric signals.

In this experimental study, we measured the seismoelectric signals excited by an acoustic multipole source in the scaled logging-while-drilling model. We put the scaled tool in a sandstone borehole to perform LWD seismoelectric and acoustic measurements. Monopole and dipole acoustic and the induced electric signals were recorded separately under exactly the same settings. The recorded acoustic and seismoelectric signals were analyzed in both time and frequency domains using a semblance method.

We found no tool mode components in the electric signals by examining both the waveforms and the time and frequency domain semblances. The underlying mechanism is the electric double layer (EDL) at the steel water interface is much weaker than the one at the formation water interface. Thus, in the LWD seismoelectric signal, there should be no component with an apparent velocity of tool mode. Since only formation acoustic modes have their corresponding components in the electric signal, we calculated the coherence of the two kinds of signals in the frequency domain. By applying the coherence curve to filter the acoustic signals, we can eliminate the tool modes and pick out the formation acoustic modes.

In the theoretical study, we developed a Pride-theory-based model for the LWD-acoustic-wave induced electric field. The electric field strength is calculated at the

electrode positions along the borehole wall, analogous to what was done in the experiment. The electric boundary conditions, which are the continuity of the electric field at the borehole wall and disappearance at the LWD tool surface, reveal the underlying mechanism in the LWD sismoelectric conversion which is also the basis of our lab experiment. The absence of the tool modes in the synthetic waveforms of the electric field coincides with what we have observed in the experimental study.

Both the experiment and the theoretical results confirm that measuring the seismoelectric signal generated by an acoustic multipole source during the LWD process can be an effective way to eliminate the tool wave contamination on the LWD acoustic measurements. This thesis research shows that seismoelectric logging-while-drilling may be a potential new method in formation property evaluation.

Thesis supervisor: M. Nafi Toksöz

Title: Professor of Geophysics

Acknowledgement

I would like to thank many people for their help towards the completion of this thesis during my two years of studying in the Earth Resource Laboratory at MIT.

First of all, I would like to thank my thesis advisor, Professor M. Nafi Toksöz for his support and guidance throughout my study at MIT. I always feel lucky to meet and work with such a reputable scientist as Professor Toksöz who offered me the chance to enter MIT as well as the field of geophysics. Besides his scientific guidance, the most important thing I learned from him is how to think and do research independently, and this thesis is a first step towards my further study in geophysics.

I would like to thank the Earth Resource Laboratory where I study and work at MIT. This environment has been a tremendous resource for both my academic study and research work. Without the well equipped Ultrasonic Lab, I couldn't have finished the experimental part of this thesis. Also, many academic events are held here weekly or monthly to let you hear the voices from both academy and industry at ERL. Besides the scientific topics, many political and social issues are discussed here that help me to better understand American life and culture. ERL has also taught me the importance of communication and cooperation which is of great importance besides the individual work.

I would like to take this opportunity to thank many of the former and current students and staff who give me a lot of technical help and spiritual encouragement. They are Youshun Sun who is always willing to share his experience of living and studying here at MIT, Burke Minsley who discussed with me on many topics and always came up with good ideas, Victoria Briggs who helped me to find useful materials on the borehole acoustic LWD, Xu Li and Rongrong Lu who gave me a lot of advice on signal processing, Samantha Grandi who always presented material in the borehole group meetings, Sophie Michelet offered a lot of friendship, Sudipta Sarkar who assists a lot with the communication within the ERL, Edmund Sze, Bill Rodi, Mark Wills, Mary Krasovec, Jonathan Ajo-Franklin who helped me to understand more about the F-K filter, Xander Campman and Joongmoo Byun. Many thanks to Liz Henderson and Sue Turbak who take good care of everyone at ERL and Linda Meinke who guarantees the smooth running of my computer.

Special thanks will be given to Dr. Zhenya Zhu. This thesis would have been impossible without his help. He taught me a lot about how to operate the laboratory experimental equipment. Through the discussion with him, I really learned a lot about borehole acoustic and electrokinetic conversion as well as the right attitude towards the scientific research. His understanding of concepts in physics really impresses me a lot, and his sincere encouragements help me to survive the difficult time in my study and work.

I also owe many thanks to Dr. Shihong Chi. I benefited a lot from his guidance on using the Fortran code for borehole acoustic modeling. He has been always generous to teach me how to solve the numerical problems in theoretical calculations. His abundant experience in borehole acoustic and petroleum engineering also helps me a lot. A lot of appreciation will be given to my office mate, Yang Zhang, for his always-there support. Our discussions range from course study to research work to daily life. His serene mentality on doing research effects me a lot.

I also acknowledge Dr. Dan Burns who is a source of encouragement and a good organizer at ERL. Thanks to him for always being ready to give help and his time spent on this thesis. I appreciate Dr. Rama Rao for his technical support. His knowledge on acoustic LWD and his Matlab codes on dispersion analysis and semblance analysis helped me greatly during the procession of the laboratory data for this thesis. I am grateful to Professor Dale Morgan for sharing his experience on how to write, organize and present a scientific work better.

Besides the people at ERL, I owe a lot of thanks to all my friends at MIT and other places in the world. I see many of them are pursuing their goals untiringly and never give up on the way. The courage and friendship they give me are so powerful. With their chats, email and phones, the life at MIT is no longer so stressful.

In the end, I can't forget to express my deepest appreciation to my family. Thanks my mother who exhibits great talent on the management of both her career and family. She witnessed my growth and shared every moment with me in my life. My father, the tutor and example for me, helps me to build up my character and set my life goals. He always encourages me to experience more and go abroad to broaden my view especially as a youth. Many thanks to my uncle and aunt who offer me the most direct and endless technical and spiritual support. Their care and regard let me strongly feel the warmth of family.

I will try to do my best in my future scientific career as a requital to all the people who have ever helped and supported me in my life.

This thesis research was supported by the Borehole Acoustics and Logging Consortium at MIT.

Contents

Chapter 1

Introduction

1.1 Objective

Borehole acoustic logging-while-drilling (LWD) for formation evaluation has become an indispensable part of hydrocarbon reservoir assessment, especially in deepwater exploration and development settings (Tang et al., 2002; Cittá et al., 2004; Esmersoy et al., 2005). However, the detection of acoustic formation arrivals [1] over tool mode contamination has been a challenging problem in acoustic LWD technology. This is because the tool mode contamination in LWD is more severe than in wireline tools in most geological environments (Tang et al., 2002; Huang, 2003).

In this thesis we propose a new method for separating tool waves from formation acoustic waves in borehole acoustic LWD. This method utilizes the seismoelectric [2] signal induced by acoustic pressure at the fluid formation boundaries.

---

[1] In this thesis, acoustic LWD measurement or signal is composed of formation acoustic waves (modes or arrivals) which are the waves propagating along the formation and tool waves (modes) which are waves propagating along the tool.

[2] Seismoelectric signal refers to the electric field induced by seismic (acoustic) waves.

The basis for seismoelectric conversion is the stronger electric double layer (EDL) that exists in most rock water systems (Ishido and Mizutani, 1981; Pride and Morgan, 1991; Loren et al., 1999). The EDL at the steel water interface of the tool, on the other hand, is rather weak (Hunter, 2001). In addition, the drilling string attached to the LWD tool is effectively grounded in field LWD operations. Therefore, there should be no contribution by the tool modes to the recorded seismoelectric signals.

Although borehole seismoelectric phenomena have been studied by several authors (Thompson and Gist, 1993; Zhu, 1997, 2003; Haartsen, 1995, 1997; Mikhailov 1998, 2000) in recent years, the seismoelectric signal generated in the LWD process and their potential applications have not been investigated. This thesis represents the first attempt in this direction of research. We first designed physical LWD experiments in the lab to collect simulated LWD monopole and dipole acoustic and seismoelectric signals in a sandstone borehole. By analyzing the acoustic and electric signals in the time and frequency domains, we can observe different signal content, which are mainly tool modes and noise. Then we applied a coherence method to pick out the common arrivals of the acoustic and seismoelectric signals, which is the pure formation modes. This method also has the side benefit of reducing the noise level in the acoustic LWD recording. This is very important for an actual field environment where the LWD recordings tend to be noisy.

To theoretically understand the seismoelectric conversion in the LWD geometry, we also calculate the synthetic waveforms for the multipole LWD seismoelectric signals based on Pride's theory (Pride, 1994). The synthetic waveforms for the electric field induced by the LWD-acoustic-wave along the borehole wall demonstrate the absence of the tool mode, which is consistent with the conclusions we get in the experimental study.

Before entering into the main body of the thesis, it is necessary to begin with a review of the fundamental physical mechanism of seismoelectric conversion and the basic operations of logging-while-drilling. These are accomplished in the next two sections. The last section of this chapter summarizes the main conclusions of this thesis research.

1.2 Seismoelectric phenomena and their geophysical application

1.2.1 Electric double layer (EDL)

When water is in contact with rock, an electric charge separation occurs at the interface: one side of the interface being positively charged and the other negatively. Such a system is called the electric double layer. Among several possible models of the electric double layer, the Gouy-Stern model, which has been improved by many authors, is generally accepted (Dukhin and Derjaguin,

1974; Bockris and Reddy, 2000). This EDL model can be described in a simplified way as follows.

When a fluid electrolyte comes into contact with a neutral solid surface, anions from the electrolyte are chemically absorbed to the wall leaving behind a net excess of cations distributed near the wall. The region is known as the electric double layer and is schematically depicted in Fig 1.1 (Pride and Morgan, 1991). The first layer of cations is bound to the anion / solid surface through both Van-der-waals and electrostatic forces. They are bound so strongly that they are assumed to be immobile. The partially fixed part of the EDL is called the Stern layer and is, in general, further divided into two layers; one is the inner Helmholtz plane (IHP) and the other is the outer Helmholtz plane (OHP). Beyond this first layer of bound cations, there is a diffuse distribution of mobile cations whose position is determined by a balance between electrostatic attraction to the absorbed layer and diffusion toward the neutral electrolyte. This diffuse part of the EDL is called Gouy diffuse layer. The Gouy-Stern is therefore a composite of a Stern layer and a Gouy diffusion zone. The separation between the mobile and immobile charge is called the shear plane. The zeta potential, ζ, is the electric potential at the shear plane, and the electric potential in neutral electrolyte (no excess charge) is defined to be zero (Pride and Morgan, 1991; Bockris and Reddy, 2000).

It is normally assumed that the diffuse distribution of mobile charge alone gives rise to the electrokinetic phenomenon and the absorbed layer does not

contribute to the electrokinetic phenomenon. The only role of the immobile charge absorbed onto the surface is to fix the value of the electric potential at the shear plane (the zeta potential). The zeta potentials are usually obtained in experimental studies. This zeta potential is the quantitative index of intensity for the EDL and differs in different material-electrolyte systems. There are numerous phenomena in which the two layers adjacent to the shear plane move with respect to each other. Examples of these 'electrokinetic phenomena' are: electro-osmosis, electrophoresis, and streaming potential (Ishido, 1981; Bockris and Reddy, 2000; Reppert et al., 2001). The zeta potential is fundamental in all these kinetic phenomena.

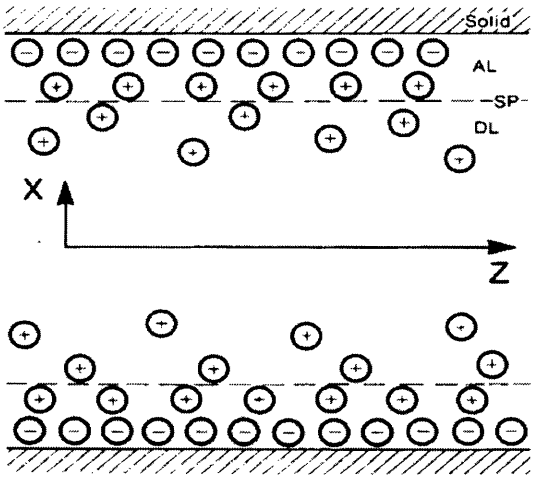

Fig 1.1 Sketch of the double layers in the planar duct. AL=absorbed layer (or Stern or Helmoholtz or immobile layer), SP=shear plane,DL=diffuse layer (or Gouy or mobile layer). The shear planes are located at $x = \pm d$ (Pride and Morgan, 1991).

1.2.2 Electrokinetic conversions in fluid-saturated porous media

When seismic waves propagate through a fluid-saturated porous media, a relative fluid-solid motion is generated (the motion of pore fluid with respect to the solid matrix). This pore fluid relative motion in rocks will induce a streaming electric field due to the electrical charges concentrated in the electric double layer (EDL) (Pride and Morgan, 1991; Mikhailov, 1998).

Previous studies have shown that two kinds of seismoelectric phenomenon can occur when a borehole seismic wave propagates along a permeable formation. One is a localized electric field induced by the pressure front of the propagating borehole seismic wave. This seismoelectric phenomena has been observed in laboratory experiments (Zhu and Toksöz, 1997) and later been theoretically modeled (Hu et al., 2000; Hu and Liu, 2002; Markov and Verzhbitskiy, 2004). The second seismoelectric phenomenon is an electromagnetic wave generated when a seismic wave hits an interface of different electrical and/or mechanical properties. The contrasting properties could be changes in physical properties (e.g. porosity, bulk, and frame moduli), changes in fluid flow permeability, or changes in fluid-chemistry (e.g. bulk free-ion concentration, PH). The EM waves generated by Stoneley waves at an isolated fracture have been observed in laboratory experiments (Zhu and Toksöz, 1998). The seismoelectric conversions due to mechanical contrasts and electrical property contrasts have also been theoretically studied (Haartsen, 1995).

Conversely, when an electric field induces relative motion of the free charges in the pore fluid against the solid matrix, the interaction between the pore fluid and the solid matrix generates an electroseismic wave. This process is the electroseismic conversion (Thompson and Gist, 1993; Pride and Haartsen, 1996). The electroseismic waves have been observed in laboratory experiments (Zhu et al., 1999) as well.

1.2.3 Geophysical applications of the seismoelectric phenomena

1. Measure the streaming potentials in situ

Streaming potential measurement has important applications in oil exploration and environmental geophysics (Segesman, 1962; Segesman, 1980; Sprunt et al., 1994). In oil exploration, it is measured as a part of the Spontaneous Potential (SP) log to identify permeable zones. In the environmental and engineering fields, the streaming potential surveys can provide information on the location, flow magnitude, and the depths and geometries of subsurface flow paths. A number of theoretical and laboratory studies have shown that streaming potentials can be used to characterize porous rocks (Fitterman, 1979; Sill, 1983). Theoretical studies have related the streaming potential coupling coefficient to the salinity and conductivity of the pore fluid and to the pore geometry of a medium. Pride (1994) also proposed a generalized theory for frequency-dependent streaming potentials in porous media. His model relates the frequency behavior of the streaming potential

coupling coefficient to the permeability. Seismoeletric phenomena provide us with a good method to measure the streaming potentials with a controlled source. Both the amplitude of the seismic wave and the induced electric signal can be measured and then utilized to estimate the streaming potential coefficient in situ to characterize rock formation (Mikhailov, 1998).

2. Characterize fluid flow property of rock formation

A number of logging methods (e.g., nuclear, nuclear magnetic resonance, Stoneley wave attenuation, etc) are currently used to characterize fluid transport properties of rock formations (Desbrandes, 1985). Recently, the borehole seismoelectric method has become a new method for characterizing fluid flow properties of a rock formation. The advantage of borehole seismoelectric logging over existing formation evaluation methods is the use of a known pressure gradient to detect the resulting flow of pore fluid (Mikhailov, 1998, 2000).

The idea of using borehole seismoelectric measurements to characterize rock formations was proposed by Ivanov in 1940s but not implemented in the field until 1996 (Mikhailov et al., 1996). In 1998, the Biot-theory-based (Biot, 1941, 1956, 1957, 1962) model developed by Mikhailov et al. predicted that the normalized amplitude of the Stoneley-wave-induced electrical field is proportional to the porosity, and the amplitude-versus-frequency behavior of the electric field depends on the permeability of the formation around a borehole. Agreement between the field measurement in fractured igneous

rocks and sedimentary rocks with the theoretical model suggests that borehole seismoelectric measurements can be used to characterize permeable formation in the field.

1.3 Acoustic logging-while-drilling (LWD)

1.3.1 Development of acoustic logging-while-drilling

Acoustic logging-while-drilling (LWD) technology was developed in the 1990's to meet the demand for real-time acoustic logging measurements for the purpose of providing seismic tie or / and acoustic porosity and pore pressure determination (Aron et al., 1994; Minear el al., 1995; Market et al., 2002; Tang et al., 2002; Cittá et al., 2004). As compared with wireline logging LWD has the advantage of measuring properties of a formation before drilling fluids invade deeply into it. Further, many wellbores prove to be difficult or even impossible to measure with conventional wireline tools, especially highly deviated wells and deepwater wells. In these situations, the LWD measurement ensures that some measurements of the subsurface are captured in the event that wireline operations are not possible or become too expensive.

The LWD acoustic technology aims at measuring the compressional and shear wave velocities of an earth formation during drilling (Tang et al., 2002). Fig 1.2 is a schematic view of an LWD multipole acoustic source built into a

drill collar. The LWD apparatus, with sources and receivers located close to the borehole wall and the drill collar taking up a large portion of the borehole, have some significant effects on borehole acoustic modes. Therefore, modeling wave propagation in the LWD environment has been the focus of several recent studies. The velocity dispersion characteristics for the formation and tool acoustic modes in LWD situations have been well studied by Rao et al., (1999, 2005) and Tang et al. (2002). The case of an off-center tool has been studied by Huang in 2003.

1.3.2 Issues with LWD acoustic measurement

The actual LWD measurement is complicated by several factors. One major influence is the noise caused by drilling and drilling mud circulation. The various vibrations of the drill string in its axial, radial, lateral, and azimuthal directions, together with the impact of the drill string on the borehole wall and the impact of the drill bit on the formation, generate strong drilling noise. Field measurements (Joyce et al., 2001) have shown that the frequency range of this noise influences the frequency range of the measurement of shear wave velocities in slow formations. The second problem is the impact of tool waves. The tool waves are strong in amplitude and always exist in the multipole LWD measurements. All these noise sources contaminate the true formation acoustic waveform, causing difficulty in the recognition of formation arrivals. When the tool is not perfectly centered the

tool modes become even more complex. Because of the complexity of collar movement during drilling, tool centralization is essentially unlikely. An off-centered quadrupole source inevitably generates some monopole and dipole components to excite tool waves along the collar (Tang et al., 2002). It is the difficulty in characterizing and removing the source of the noise that has motivated the research in this thesis.

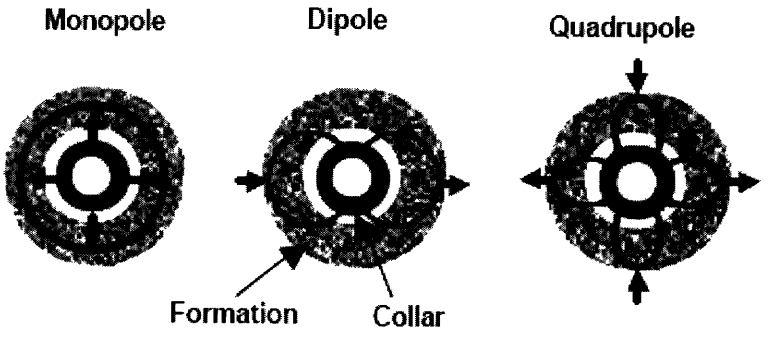

Fig 1.2 Azimuthal wave-amplitude variation pattern for the monopole, dipole and quadrupole sources in connection with the LWD model (Tang et al., 2002).

1.4 Thesis outline and summary of results

In this thesis, borehole monopole and dipole LWD acoustic and seismoelectric phenomena are first investigated by experimentally obtaining the data in the lab followed by performing a series of analyses and comparisons. Then theoretical modeling of the LWD-wave-induced electric field along the borehole wall, which is made of a homogenous, elastic formation, is accomplished. From the theoretical calculation, we can better

understand the mechanism in the LWD seismoelectric conversion and further prove the absence of the tool modes in the LWD seismoelectric signals. The main thrust of this thesis is the utilization of the difference between acoustic and seismoelectric signals to eliminate the tool waves in the acoustic LWD data.

In Chapter 2, we first introduce the various acoustic wave modes existing in monopole and dipole LWD by calculating the theoretical velocity dispersion curves. We then review the seismoelectric signals that can be generated by the acoustic wave in the borehole based on previous studies. Afterwards, we describe the experimental setup, equipment, and borehole models used for the laboratory LWD acoustic and seismoelectric measurements.

In Chapter 3, we present and analyze our recorded acoustic and seismoelectric signals. First we describe the array processing methods applied to the experimental data in the time and frequency domains. Then we demonstrate a noise reduction technique used to enhance the signal to noise ratio for the seismoelectric data. We then study the acoustic properties of our scaled multipole tool by exciting the tool wave in a water tank, in the absence of a formation. We will identify the various monopole, dipole acoustic wave modes of different velocities and examine their dispersion properties by comparing the frequency domain semblance with the theoretical dispersion curves calculated in Chapter 2. For the seismoelectric study, we will

experimentally demonstrate that the seismoelectric signal generated by the tool wave at the steel-fluid interface is indeed fairly weak due to the low intensity of the EDL at the steel-fluid interface.

Another focus of Chapter 3 is to study the difference in information content between the LWD acoustic and seismoelectric signals. The comparison shows that there is no tool wave velocity component in the LWD seismoelectric signal because the EDL at the steel-fluid interface is very weak and the tool is effectively grounded during the actual LWD process. After attaining that conclusion, we calculate the coherence curve for the LWD acoustic and seismoelectric signals in frequency domain. The high-coherence frequency band corresponds to the formation acoustic modes. Conversely, the low coherence frequency range corresponds to the tool modes and noise. Thus, we can utilize the LWD seismoelectric signal to separate the tool waves from the formation arrivals in acoustic signals by simply applying a filter obtained from the correlation function between the seismoelectric and acoustic signals.

In Chapter 4, we develop a Pride-theory-based model for the LWD-acoustic-induced electric fields. The electric field potential and streaming current densities both along the borehole wall and within the borehole are determined once the acoustic field is known. The electric field boundary conditions - the continuity of the electric field potential and the radial streaming current density at the borehole wall; the vanishing of the electric field at the LWD tool surface - reveal the basic mechanisms in the

LWD seismoelectric conversion. The acoustic pressure is calculated at the receiver transducer positions along the LWD tool rim. The electric field strength is calculated at the receiver electrode position along the borehole wall similar to the laboratory experiment. Synthetic waveforms are calculated by using the same borehole geometry and medium parameters scaled to the lab experiment borehole, which is a fast formation. The same kind of calculation is also made in a slow formation. The various monopole and dipole modes can be recognized in the waveforms and in the time domain semblance. The time derivative of the acoustic pressure can match the electric field strength very well to show the $\pi/2$ phase shift (as shown in equation 4.4). Most important is the absence of the tool modes in the LWD synthetic waveforms which is consistent with our experiment results.

The main contributions of this thesis are:

1. The study of the borehole seismoelectric phenomenon in the LWD geometry, it is the first recognition of the potential benefit of simultaneous LWD acoustic and seismoelectric measurements. The experimental procedure and results show encouraging signs for further development of LWD seismoelectric measurements.

2. This thesis presents a new method in tackling the long existing LWD acoustic logging problem of tool wave contamination on the formation acoustic waves by utilizing the mechanism of seismoelectric conversion.

3. The correlation of the LWD seismoelectric signal and the acoustic signal provides a filter to remove the tool modes and preserve the formation acoustic wave modes. Another benefit of this method is the reduction of the noise level in LWD acoustic measurement.

4. The theoretical modeling of the LWD-acoustic-wave induced electric field reveals the basic mechanism in the LWD seimoelectric conversion. The synthetic LWD electric waveforms confirm the absence of tool modes, which is consistent with the experimental results.

Chapter 2

LWD acoustic and seismoelectric measurements in a scaled laboratory experiment

In this Chapter we discuss the experimental setup for our laboratory monopole, dipole LWD acoustic and seismoelectric measurements. First, we establish the monopole and dipole LWD acoustic modes in the lab borehole and tool geometry by calculating their theoretical dispersion curves. We then describe the mechanism of seismoelectric conversion in a fluid-filled borehole, especially under the multipole acoustic LWD excitation. After these theoretical introductions, we describe the experimental setup for the lab measurement. This includes the structure of the scaled multipole tools and their working combinations, the borehole models, and the laboratory measurement procedure.

2.1 Acoustic multipole source in fluid-filled borehole

The use of axially symmetric sources such as a monopole source and axially non-symmetric sources such a dipole source has become routine in acoustic logging (Schimitt, 1986, 1989; Schimitt and Cheng, 1987; Chen and Eriksen, 1991; Tang and Cheng, 1993; Tang and Wang et al., 2002). Different types of acoustic sources can generate borehole acoustic waves with different particle displacement patterns and dispersion characteristics. To construct a multipole source of order n, $2n$ point sources are distributed periodically in a horizontal plane along a circle of radius r_0 and alternate in sign as shown in Fig 2.1.

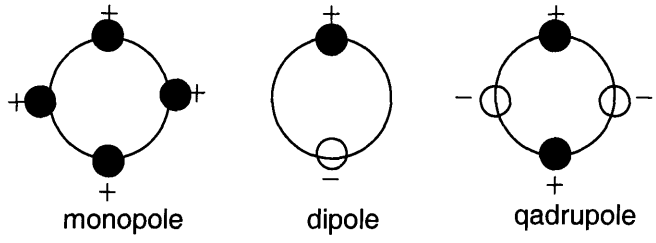

Fig 2.1 Monopole, dipole and quadrupole source

The displacement potential field of a point source can be obtained by solving the wave equation in the fluid. To synthesize the wave field due to a multipole source, we could sum the wave fields due to each source (Biot, 1952; Peterson, 1974; Roever et al., 1974; Tsang and Rader, 1979; White, 1983; Kurkjian and Chang, 1986). By constructing the acoustic wave field in the borehole and matching the boundary conditions at the fluid-solid interface, we can obtain the response of the formation to the multipole sources.

2.2 Borehole acoustic modes in logging-while-drilling

The need for measuring formation acoustic properties during drilling calls for modeling wave propagation in the LWD environment (Tang et al., 2002). Understanding the LWD acoustic-wave phenomena can help the design of an LWD acoustic tool as well. We can calculate the wave velocity dispersion curves for all the modes in LWD by using the acoustic wave theory for a multi-layered system (Tsang and Radar, 1979; Cheng and Toksöz, 1981; Tang and Cheng, 1993; Hsu et al., 1997; Nolte et al., 1997; Rao et al., 1999, 2005; Tang and Cheng, 2004). The model parameters of our laboratory tool and the borehole, which is in a fast sandstone formation, are shown in table 2.1. The tool ID is 0.04 m, tool OD is 0.10 m and borehole radius is 0.17 m. By examining the phase velocity curves as a function of frequency for the various wave modes as shown in Figs 2.2 and 2.3, we can observe the modal excitation of acoustic monopole and dipole sources.

	P-velocity	S-velocity	Density	Outer radius
Inner fluid	$1500 m/s$	-------	$1000 kg/m^3$	0.024m
Tool (Composite)	$4185 m/s$	$2100 m/s$	$7700 kg/m^3$	0.085m
Outer fluid	$1500 m/s$	-------	$1000 kg/m^3$	0.11m
Formation	$4660 m/s$	$2640 m/s$	$2100 kg/m^3$	∞

Table 2.1 LWD lab borehole model used in theoretical modeling

2.2.1 Monopole modes

For an axi-symmetric monopole source, the period equation will yield the following wave modes:

Pseudo-Rayleigh wave: Pseudo-Rayleigh only exits in a formation with a shear wave velocity higher than the fluid acoustic velocity (Cheng and Toksöz, 1981; Tang and Cheng, 2004). As Fig 2.2 shows, the Pseudo-Rayleigh wave is strongly dispersive and has a cutoff frequency below which it cannot exist. Its phase velocity peaks at the formation shear velocity at the cutoff frequency and drops to the fluid velocity at high frequencies. We can see the 1^{st} and 2^{nd} order Pseudo-Rayleigh wave modes in our borehole models.

Stoneley wave: Stoneley wave is the interface wave traveling along the borehole interface. The Stoneley wave, unlike Pseudo-Rayleigh, exists in both fast and slow formations and at all frequencies. Its phase velocity increases with frequency in fast formation. The introduction of the steel tool will reduce the low-frequency limit of the Stoneley phase velocity considerably.

Monopole tool mode: The property of tool mode largely depends on the material and geometry of the tool. For our experimental tool, the monopole tool mode only exits in the low-frequency range with a phase velocity faster than the formation shear velocity.

2.2.2 Dipole modes

Flexural wave: The flexural wave in a fast formation has similar characteristics as the Pseudo-Rayleigh wave in the monopole case (Fig. 2.3), attaining the formation shear velocity at low frequencies.

Dipole tool mode: For our experimental tool, the dipole tool mode exists in the whole frequency range and has a very low velocity limit at the low-frequency end.

Higher order modes: When the excitation frequency is very high, it is easy to excite the higher order modes such as the hexapole modes. These higher order modes have cutoff frequencies and their phase velocities decrease when frequency increases (Chi et al., 2005).

2.3 Seismoelectric phenomena in a borehole

The idea of using borehole seismoelectric measurements to characterize rock formation in-situ was suggested by Ivanov (1940). The advantage of borehole seismoelectric logging over existing formation evaluation methods, is its ability to detect fluid flow in a porous formation induced by a pressure gradient (Mikhailov, 1998). Experimental studies of electrokinetic conversions in fluid-saturated borehole models have been carried out by Zhu and Toksöz (1996, 1997, 1999, 2003) and Zhu et al. (1999, 2000). Field measurements of electric fields induced by a borehole Stoneley wave were made by Mikhailov et al. (2000) to detect fractured (permeable) zones intersecting the borehole.

Two kinds of seismoelectric phenomena of which one is the localized electric field and the other is the radiated electromagnetic (EM) wave are predicted by theory and verified by experiments.

2.3.1 Localized electric field induced by acoustic wave in homogenous permeable formation

When seismic waves propagate through a homogenous fluid-saturated porous media, the pressure gradient will cause the movement of fluid and the excess charge in the pore fluid (Mikhailov, 1998, 2000). The induced current produces an electric field localized around the wave pulse. The electric field occurs synchronously with the seismic waves. Thus, this localized electric field has a velocity of the seismic wave (Zhu et al., 1997, 1999; Mikhailov, 1998).

2.3.2 Electromagnetic wave induced by acoustic wave at an isolated fracture

When the seismic waves propagate through an interface between two different porous media, a radiating electromagnetic wave will be generated at the interface. In this case the incident seismic waves cause an unbalanced dynamic charge separation, serving as the source for the radiated electromagnetic waves (Haartsen and Pride, 1997). These EM waves originate from the boundaries separating layers of different elastic or electric properties.

They propagate with the EM velocity in the formation, which is "infinite" as compared with the seismic velocity. EM waves generated by Stoneley waves at an isolated fracture have been observed in laboratory experiments (Zhu and Toksöz, 1998). Field recording of this electromagnetic wave has been reported by Mikhailov (1998).

2.4 Experimental setup for multipole acoustic LWD measurement in a scaled borehole

In LWD multipole acoustic logging, both the source and the receiver transducers are tightly mounted on the drill collar. This attachment results in the receivers recording a tool mode propagating along the drill collar. The tool mode can interfere with the acoustic fields propagating along the formation. To simulate the LWD measurement, we built a scaled multipole acoustic tool composed of three parts: the source, receiver, and a connector (Zhu et al., 2004). Working in the ultrasonic frequencies the tool is put into a scaled borehole to measure the monopole and dipole acoustic waves, in one case with the connector and in the other case without. In the following sections, we explain the structure of the scaled tool and its working combinations.

2.4.1 Structure of a scaled multipole tool

Our laboratory LWD tool includes three sections: the source, the receivers, and the connector. Both the source and receiver acoustic transducers are made of PZT crystal disks of 0.635cm in diameter and 0.37cm in thickness. The dimension of the tool is shown in Fig 2.4.

The source is made of four separate crystal disks shown in the B-B profile of Fig 2.4. The arrows on the disks indicate their piezoelectric polarization. Each disk has two electrodes attached to it; the eight electrodes are connected to a switch. Using the switch to change the electric polarization applied on each crystal disk, we can achieve a working combination to simulate a monopole or dipole source.

The receiver section is composed of six pairs of crystal disks at six different locations. The polarizations of each disk pair are shown in the A-A profile of Fig 2.4.

The connector section is made of a steel pipe threaded at each end. The source and receiver sections are tightly connected by this steel pipe to simulate the drill-string connection in LWD. For some of the experiments, we removed the connector in order to eliminate the tool modes which propagate from the source section, through the connector, to the receiver section.

2.4.2 Working configurations of the tool

By changing the electric polarization of the source PZT disks and by combining the signals received by the receiver disk pairs, we are able to mimic

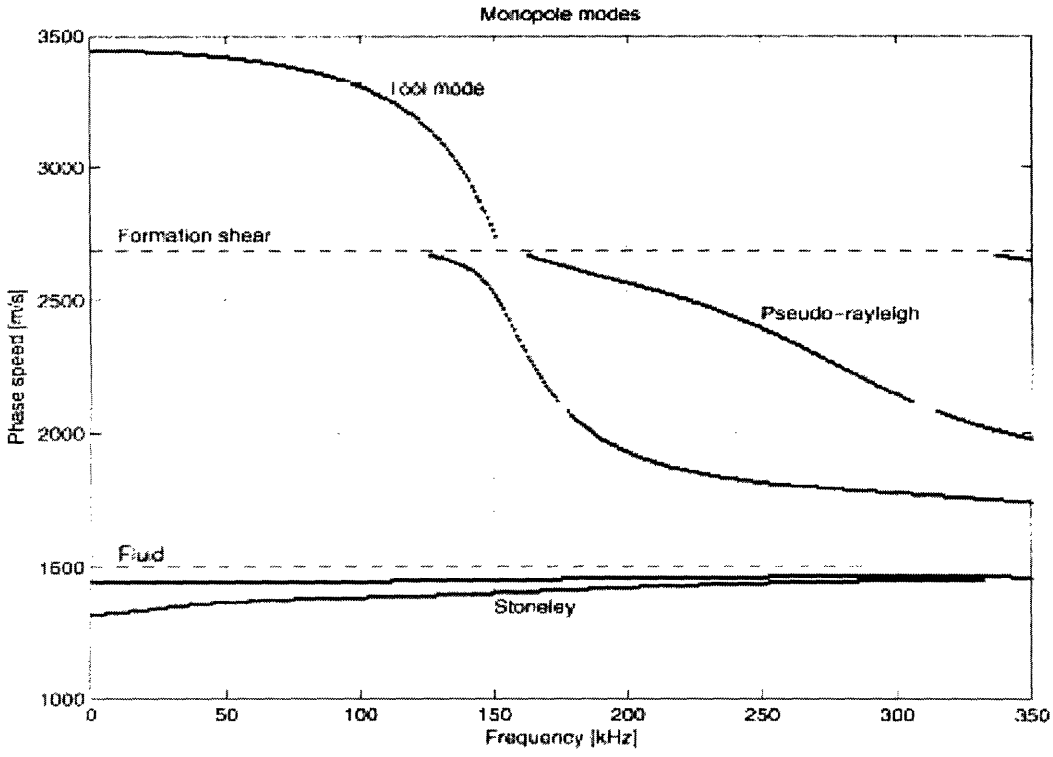

Fig 2.2 Dispersion curves for monopole wave modes in LWD lab borehole

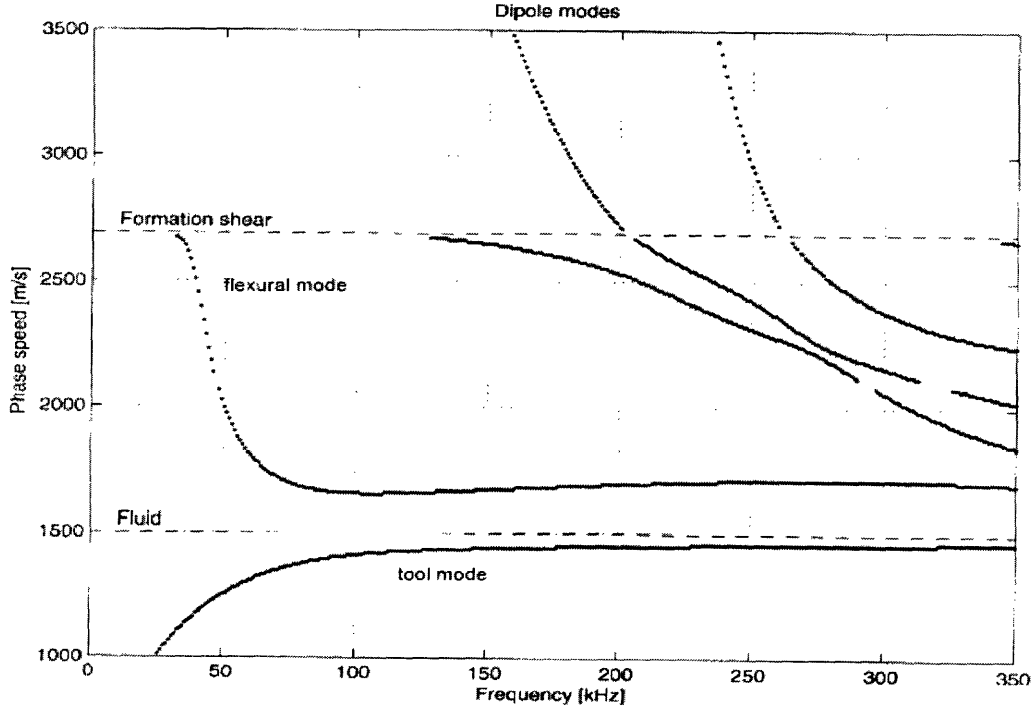

Fig 2.3 Dispersion curves for dipole wave modes in LWD lab borehole

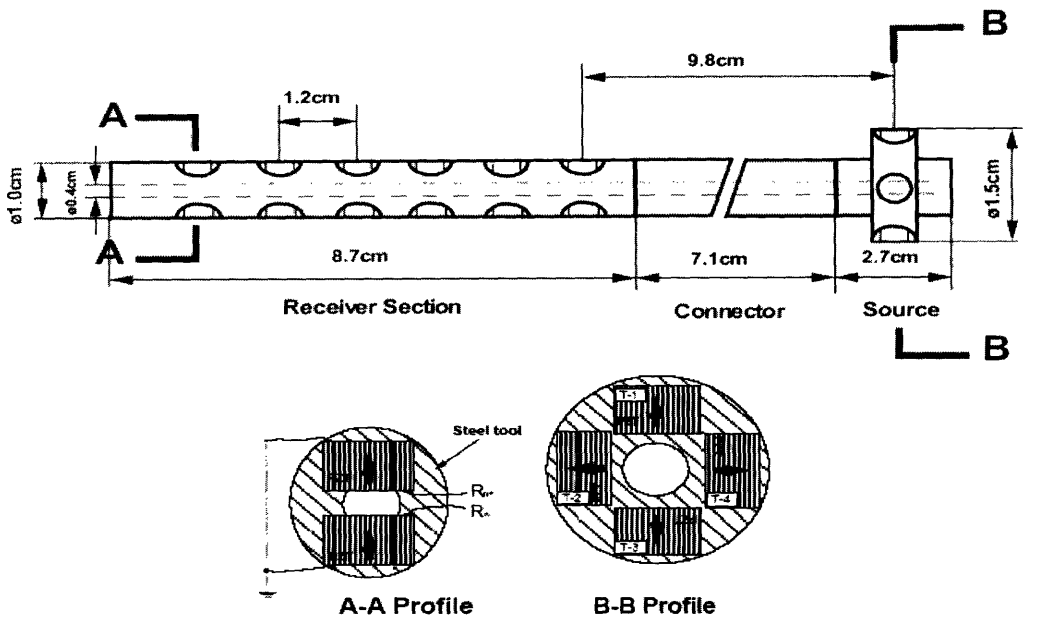

Fig 2.4 Schematic diagram of the scaled multipole logging tool. The arrows indicate the polarization of the PZT disks (Zhu et al., 2004).

a working system of acoustic logging sources. When the piezoelectric polarization of the source transducer is consistent with the positive pulse of the source signal, the phase of the acoustic wave is also positive. The polarization of the received acoustic field is the same as the piezoelectric polarization of the receiver transducer. The working combinations of monopole and dipole systems are shown in Fig 2.5.

During measurements, we used a switch to change the working mode from monopole to dipole. This allows us to conduct the multipole logging without changing or moving the tool position. Therefore, the experiment results can be compared under the identical conditions.

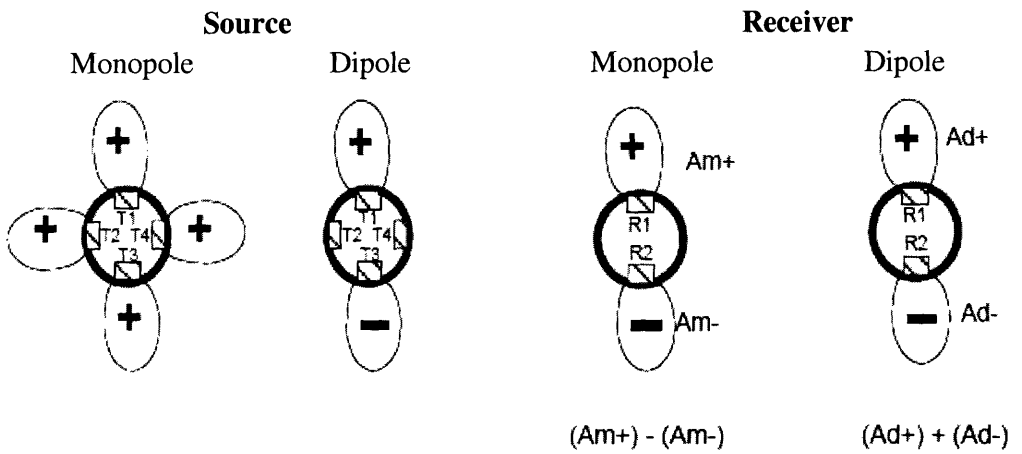

Fig 2.5 Schematic diagram of the working modes of the multipole logging tool. The "+" and "-" indicate the polarization of the electric signals in the source and the polarization of the PZT crystals in the receiver (Zhu et al., 2004).

2.4.3 Experiment borehole model

The experiment borehole we use is an isotropic hard formation – sandstone. The sandstone block has a length of 30cm, a width of 29cm, and a height of 23cm. The diameter of the borehole is 1.7cm. The P- and S-velocities are all higher than the borehole fluid velocity. All the velocities are shown in table 2.1. Schematics of the borehole model are shown in Fig 2.6.

2.5 Experimental setup for multipole seismoelectric LWD measurements

To measure the seismoelectric signal, we need to change the receiver section from acoustic transducers to electrodes. The electrodes used for this experiment are point electrodes of 1.0mm in diameter. Thus, each electrode on the electrode array can only detect the electric field around it.

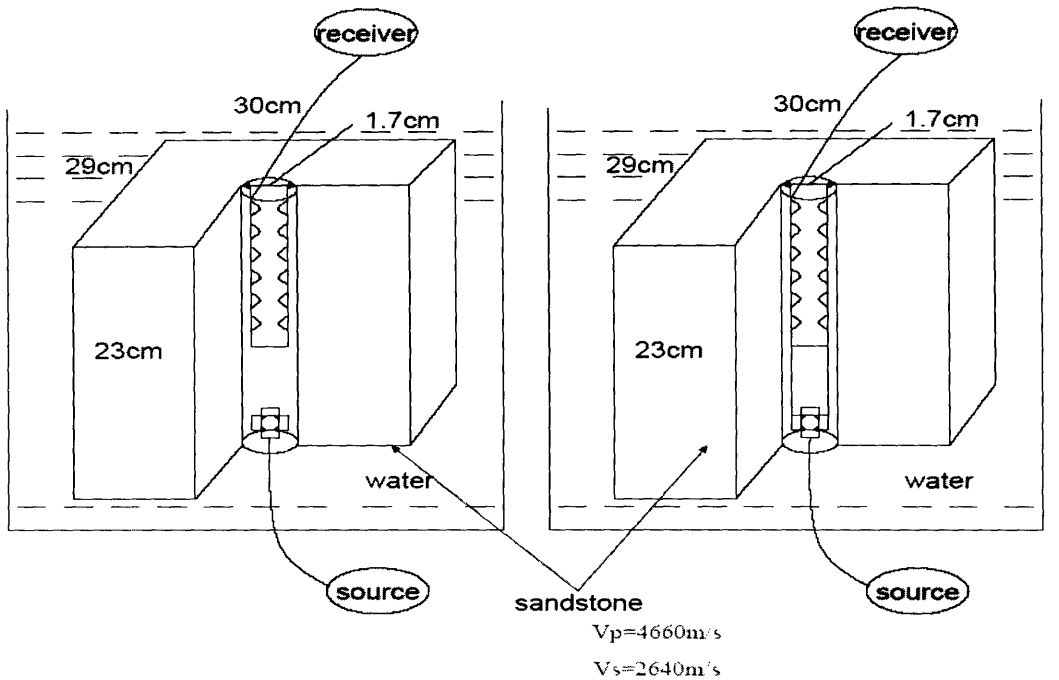

Fig 2.6 Laboratory borehole model (Vp stands for the formation P wave velocity and Vs stands for the formation S wave velocity).

The multipole tool used to measure seismoelectric signals is also composed of three parts: source, receiver and connector. The source section and the connector are exactly the same in structure and size as in the acoustic case. The only change is the replacement of the array of the six pairs of transducers by an array of six pairs of electrodes spaced at the same interval. The holes in which the electrodes are imbedded are filled with sand and glued by epoxy. The surface is covered with conducting glue and connected to the steel tool. The acoustic transducer is embedded in the logging tool as shown in Fig 2.4 to measure the acoustic pressure at the tool rim. The electrodes are protruding from the tool surface (Fig 2.7) and are close to the borehole wall to measure the strength of the localized electric field at the borehole wall.

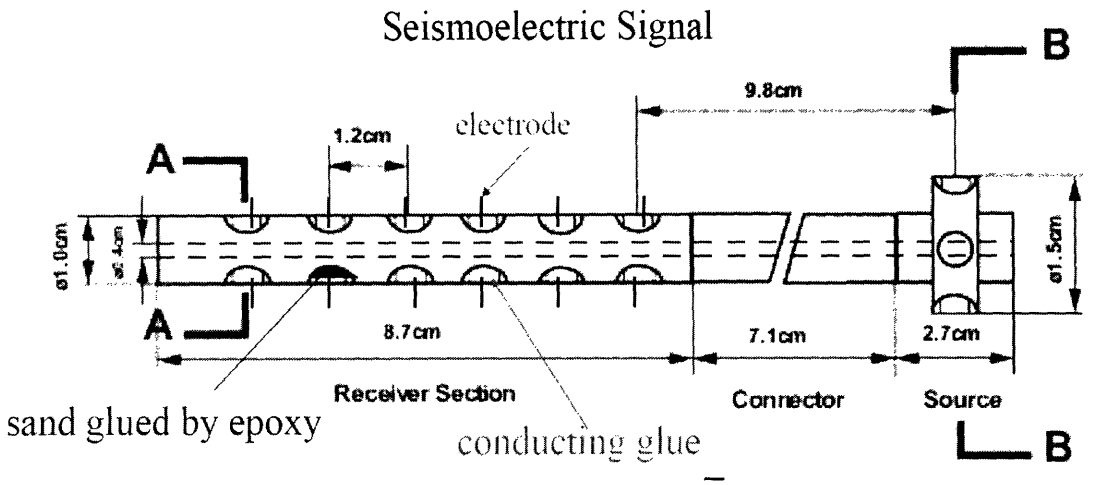

Fig 2.7 Schematic diagram of the scaled lab multipole tool in seismoelectric measurement.

2.6 Experiment mechanism and procedure

2.6.1 Electric double layers in LWD measurements

It is generally accepted that the electric double layer (EDL) is the basis for the electrokinetic conversion (Pride and Morgan, 1991; Loren et al., 1999). For our sandstone borehole model, an EDL is developed at the borehole wall. When the acoustic waves hit the borehole wall, a localized electric field is generated and the electrode detects this electric field. Since the conductivity of the borehole fluid is very low, the recorded voltage between the electrode and ground can represent the electric field generated at the borehole wall. The difference between rock and metal is that the former has strong intrinsic dipoles while the steel can sustain only a weak induced dipole (Bockris and Reddy, 2000; Hunter, 2001). As a result, the double layer is much weaker in intensity in case of steel than in case of rock. In the seismoelectric signals, what we record is purely the electric field excited by the formation acoustic

waves propagating along the borehole wall and with the apparent velocities of formation acoustic modes. No electric component propagating at the apparent speed of tool wave can be observed in the electric signals.

2.6.2 Laboratory measurement procedure

Before starting an experiment the sandstone borehole model with a vertically drilled hole is lowered into a water tank. The source and receiver sections are put into the borehole from two sides with, or without, the connector in place. The source side is connected to a high voltage generator and the receiver side to a preamplifier and a filter before being displayed on an oscilloscope. The working system is shown in Fig 2.9. The High Power Pulse Generator generates a square pulse with a duration of 10us. This means that the source wavelet is a square wave with a center frequency of 100 kHz. The excitation voltages for the measurements vary between 5 volts and 750 volts. The sampling rate is 500 ns. For each trace we record 512 points. The filter range set from 300 Hz to 500 kHz is broad enough to include all the dominant acoustic and electric modes.

We first measure the monopole and dipole tool modes for calibration of our laboratory tool. Then we take measurements in the borehole to record monopole and dipole acoustic waves when the tool is operated with or without the connector. After finishing recording of the measurements for the acoustic signals, the acoustic receiver transducers are replaced by electrodes to make

the seismoelectric measurements. We first put the grounded tool into the water tank again to test if any seismoelectric signal can be observed. In the end, we focus on the seismoelectric signal in the sandstone when the tool is used with or without the connector.

In total seven different measurements are made and all signals are analyzed in both time and frequency domains using a semblance method. The waveforms and analysis results will be presented in the following sequence in Chapter 3:

① tool waves in the water tank

② acoustic signals without the connector

③ acoustic signals with the connector

④ seismoelectric signals with the grounded tool in the water tank

⑤ seismoelectric signals without the connector in sandstone model

⑥ seismoelectric signals with the connector in sandstone model

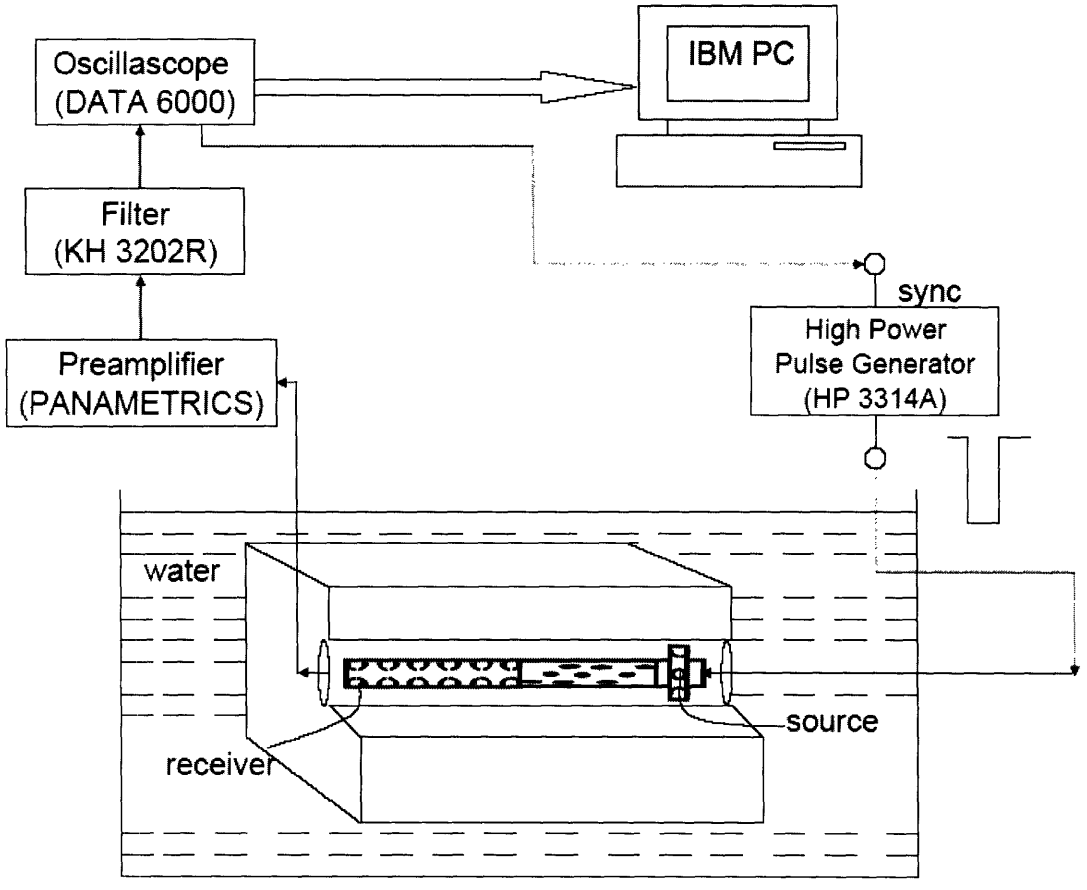

Fig 2.9 Schematic diagram of the experiment working system (The source wavelet from the High Power Pulse Generator is a square wave).

Chapter 3

Analysis of laboratory experiment acoustic and seismoelectric signals

In this Chapter we analyze the acoustic and seismoelectric signals obtained in our laboratory experiments to achieve three objectives: 1) study of the acoustic LWD signal generated by our scaled lab tool in the lab borehole geometry; 2) understanding the seismoelectric phenomena in the LWD process; 3) investigating the potential application of the LWD seismoelectric signals. First we introduce an array processing method used to analyze the recorded acoustic and seismoelectric signals and a noise reduction method to analyze the electric signal. We then assess the impact of tool modes on LWD acoustic measurements. Finally, we observe the difference between LWD acoustic and seismoelectric signals and make use of the seismoelectric signal as a filter to separate out the tool modes from the formation acoustic modes in acoustic LWD signals.

3.1 Array processing methods in time and frequency domain

Modern acoustic logging tools contain an array of receivers for recording acoustic waveform data (White and Zechman, 1968; Cheng and Cheng, 1996; Tang and Cheng, 2004). Array processing methods can be used to detect the various wave modes embedded in the waveform and calculate their velocity dispersion characteristics in a borehole. We use the semblance method to analyze the experimental data. This method can be applied in both time and frequency domains (Rao et al., 1999, 2005).

3.1.1 Time domain semblance

Time domain semblance algorithm searches for all arrivals received by the array and locates the appropriate wave arrival time and slowness values that maximize the coherent energy in the array waveforms. The coherence is defined as (Kimball and Marzetta, 1984)

$$\rho(s,T) = \frac{\int_{T}^{(T+T_w)} \left| \sum_{m=1}^{N} X_m(t + s(m-1)d) \right|^2 dt}{N \int_{T}^{(T+T_w)} \sum_{m=1}^{N} \left| X_m(t + s(m-1)d) \right|^2 dt} \tag{3.1}$$

The acoustic array is composed of N receivers with a spacing of d. $X_m(t)$ represents the acoustic time signal at the mth receiver. A set of time windows defined by the center position T and length T_w is applied to the waveforms. The time window slides through the waveform at a certain time

increment (usually half of the T_w). For a range of values of arrival time and slowness, the scalar semblance is computed for the windowed portion. We can find some values of T and s, say (s_k, T_k), which maximize the semblance coherence function and obtain a semblance surface in the time-slowness plot. These peak semblance values mark the arrival time and the slowness of the acoustic wave modes in the array data (Tang and Cheng, 2004).

3.1.2 Frequency domain semblance

Frequency domain semblance is commonly used to estimate the velocity dispersion characteristics of the guided waves from array wave data. I use the method developed by Nolte et al. (1997) and Rao et al. (1999, 2005) to weight the semblance (or coherence function) of the array data. This method processes a frequency by weighting the data over neighboring frequencies and searches the peak of weighted semblance function over a range of slowness values to find the actual number of wave modes. The spectral semblance is defined as (Tang and Cheng, 2004)

$$\rho(\omega, s) = \frac{\left| \sum_{n=1}^{N} X_n^*(\omega) z^{n-1} \right|}{\sqrt{N \sum_{n=1}^{N} X_n^*(\omega) X_n(\omega)}} \tag{3.2}$$

where $z = \exp(-i\omega s d)$, $s(\omega)$ is the slowness at frequency ω and d is the receiver spacing, the total expression for z denotes the wave propagation. The wave mode traveling at a distinct slowness $s_k(\omega)$ across each receiver in

the array is $X_n(\omega) = h_k z_k^{n-1} = h_k(\omega)\exp(-i\omega s_k(n-1)d)$ where $h_k(\omega)$ the amplitude of the kth wave mode. Maximizing $\rho(\omega, s)$ as a function of s_k for different frequencies will generate the dispersion curves. To enhance the data information and reduce noise, we first resample the spectral data to obtain denser data points and then try to maximize a weighted semblance function defined as

$$F(\omega_l, s) = \sum_{j=l-m}^{l+m} W(\omega_j, \omega_m)\rho(\omega_m . s) \tag{3.3}$$

where ω_l stands for the re-sampled frequency, $W(\omega_j, \omega_m)$ is a Gaussian weight function given by

$$W(\omega_j, \omega_m) = \exp(-\frac{(\omega_m - \omega_j)^2}{2\sigma^2}). \tag{3.4}$$

The number of neighboring points to be weighted over is controlled by σ. Usually σ is set to be $4\Delta\omega$, where $\Delta\omega$ is the increment of re-sampled data.

3.2 Noise reduction in seismoelectric data

The electric data in the experiment is recorded by the point electrodes exposed in water. The signal is rather weak, therefore can be contaminated by the ambient electric fields (Butler and Russell, 1993, 2003; Russell et al., 1997). This ambient noise not only contaminates the electric waveforms but also reduces the ability of the semblance method to recognize the wave modes. In order to reduce noise and enhance the signal to noise ratio (SNR) of the

electric signal, steps need to be taken both during the data collection process and during analysis.

To reduce random noise, we sum the repeated measurements. The averaging function of the oscilloscope is used for summing. Each trace in electric array data is the average of 512 sweeps. Good shielding to eliminate the outside noise is also very important for weak signal detection. Some good practices include the following: effectively grounding the computers, oscilloscope, and the shielding line of the point electrode; placing the transducers and electrodes completely in water; shutting down unnecessary electric sources; grounding the water tank, etc.

Besides random noise, we also have a large synchronous signal from the source and a DC component in the electric recordings. This synchronous signal is large in amplitude and appears in front of the wave train so that a lot of useful modes may be buried in the large noise. Fortunately, the source noise does not have a phase move-out over the receiver array, while the seismoelectric signals do. We can subtract the mean value of the six source – receiver offsets traces from each individual trace to eliminate this noise. The DC component can be eliminated with a high-pass filter for each trace seperately. The recorded seismoelectric signals before and after noise reduction are shown in Fig 3.2 for the monopole case and Fig 3.3 for the dipole case. All the traces in Fig 3.2 and 3.3 are normalized with the same scaling factor.

3.3 Tool waves in the water

In order to understand the properties of monopole and dipole tool modes of our specific scaled multipole tool, we first conduct measurements by putting the tool with and without the connector into the water tank, in the absence of a borehole and formation, as shown in Fig 3.1. Case A has been studied by Zhu et al. (2004) and we do not repeat it here. Since the acoustic impedance difference between the steel and water is large, no tool wave can be recorded when the connector is not present.

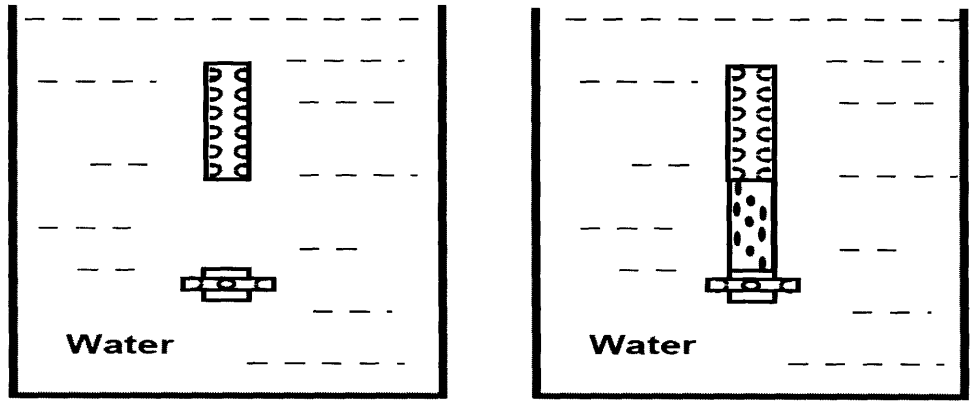

Fig 3.1 Measurements in a water tank without (A) or with (B) connector (Zhu et al., 2004).

In case B, we make the measurements in water tank with the connector and obtain the monopole tool wave (speed at $3500 m/s$) and the dipole tool wave (speed about $800 m/s$). These results are consistent with the theoretical dispersion curves we calculated in Fig 2.3 and Fig 2.4. The waveforms of monopole and dipole tool modes and their time domain semblances are shown in Fig 3.4.

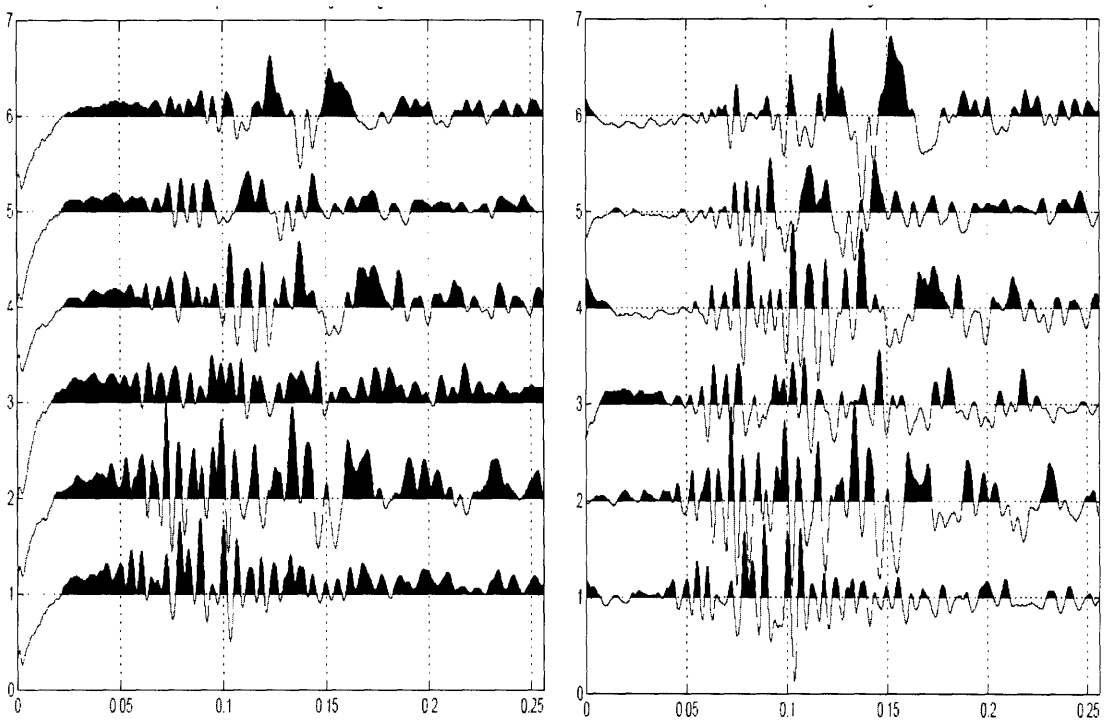

Fig 3.2 Seismoelectric signals before (left) and after (right) noise reduction for monopole.

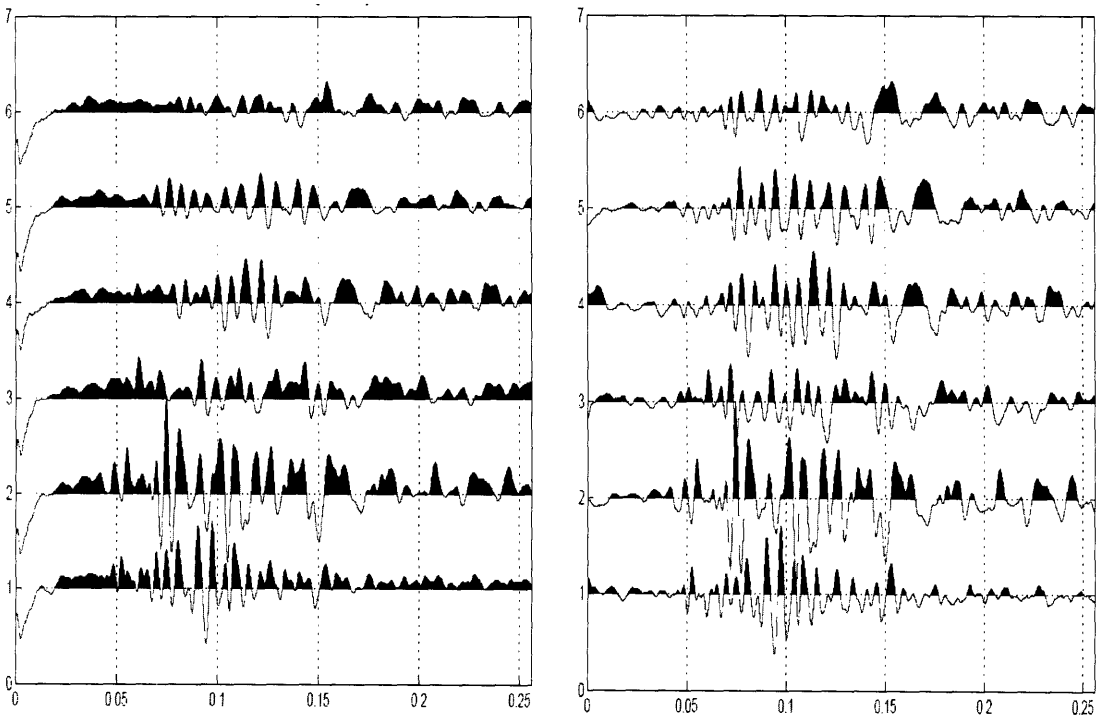

Fig 3.3 Seismoelectric signals before (left) and after (right) noise reduction for dipole.

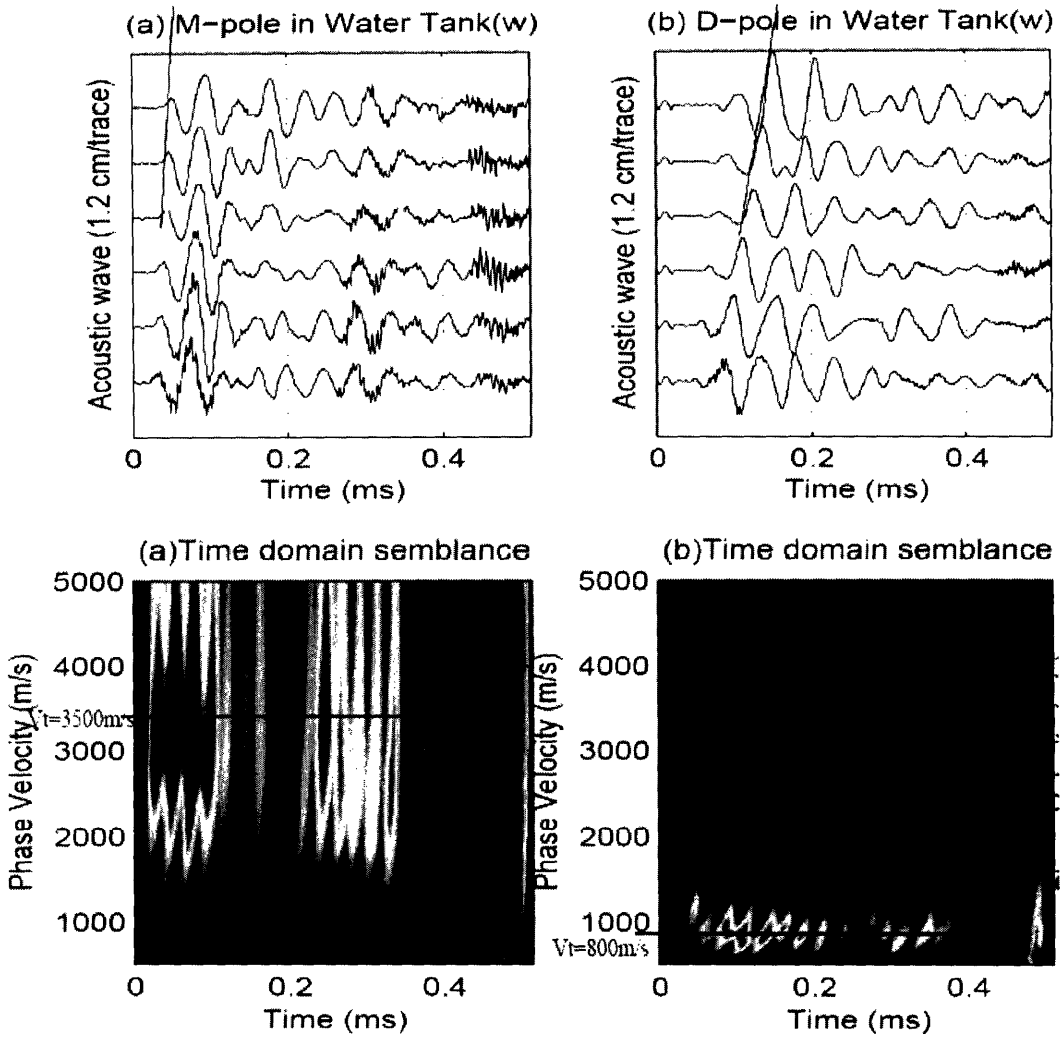

Fig 3.4 Monopole (a)(left) and Dipole (b)(right) tool wave waveforms and their time domain Semblance. (Vt stands for lab tool wave velocity.)

3.4 Acoustic signals, tool without the connector in the borehole

To validate our scaled lab tool and its working combinations we perform logging measurements in the water–saturated sandstone borehole using the tool without the connector. The waveforms and time and frequency domain

semblances of the monopole and dipole modes are shown in Fig 3.5 and Fig 3.6, respectively.

From the monopole waveforms in Fig 3.5, we can observe the early arriving P- and a S-waves corresponding to the peaks in the time domain semblance. Following the early arrivals are the dispersive wave trains, including the Pseudo-Rayleigh wave and the Stoneley wave. The Stoneley wave is relatively weak in this case because the transducer used in the experiment has a high frequency response while the Stoneley wave energy mostly concentrates in the low frequency range.

The dipole waveforms are much simpler than monopole waveforms. A dispersive flexural wave can be observed with a speed lower than the formation shear velocity in the time domain semblance and approaching the formation shear velocity at the low frequency.

3.5 Seismoelectric signals with the tool in the water

To understand the EDL at the steel fluid interface more intuitively, we measure the seismoelectric signals by putting the scaled multiple tool in the water tank. This is exactly the same setup as the measurement of tool waves in the water with the connector shown in (Fig 3.3B). The electric signals generated at the steel water interface are shown in Fig 3.7A for the monopole tool wave and Fig 3.7B for the dipole tool wave.

The electric records taken at the tool water interface are very weak due to the low density of the EDL at the steel water interface and the grounding of the steel tool. Fom the time domain semblances of those seismoelectric signals at the steel fluid interface in Fig 3.7C and 3.7D, no mode is observed. Thus, the LWD seismoelectric signal should contain no tool mode contribution.

3.6 LWD acoustic and seismoelectric signals in the sandstone borehole

At this point, we have validated our scaled laboratory tool as a multipole acoustic source, studied the acoustic property of the laboratory tool, now we will focus on the difference between the LWD acoustic and seismoelectric signals in the sandstone borehole model. As pointed out previously, the seismoelectric signal excited in the acoustic LWD process should contain no signals with the apparent velocity of the tool modes.

We now examine the two kinds of signals for monopole (Fig 3.8) and dipole (Fig 3.9) excitations using time domain and frequency domain analysis. The theoretical dispersion curves calculated in Chapter 2 are superposed on the frequency domain semblance to help identify various wave modes. From the acoustic waveform we can clearly see a monopole tool wave coming between P and S wave and a low frequency dipole tool wave coming in the late part of the wave train. In the time domain semblance we can observe the peaks at the monopole and dipole tool waves. In the seismoelectric data, tool modes do not

exist. This is especially clear in the frequency domain semblance, where the monopole and dipole tool modes are absent. These results show that by measuring the seismoelectric signal during the logging-while-drilling process, we can potentially eliminate the effect of tool modes.

Based on the experiments, we have two ways to eliminate tool waves: one is to remove the connector between the source and the receiver, the other is to collect the LWD seismoelectric signals. By comparing the LWD acoustic and seismoelectric signals collected with the connector to the acoustic signals taken when the tool was without the connector, as shown in Fig 3.10 and Fig 3.11, we can see the usefulness of seismoelectric measurements. Collecting the seismoelectric signal is a good way to remove the tool modes in real LWD.

3.7 Application of seismoelectric signal induced in acoustic LWD

Based on the laboratory experiments we conclude the following:

LWD acoustic signal = Formation acoustic waves + Tool waves + Noise

LWD SEL signal = Formation acoustic wave induced electric signals + Noise.

In field acoustic LWD operation, the tool modes can have velocities close to the formation velocities for some formations. Therefore, the detection of formation arrivals can be hampered by tool mode contamination. When the LWD tool departs from the centralized position, the tool contamination can be

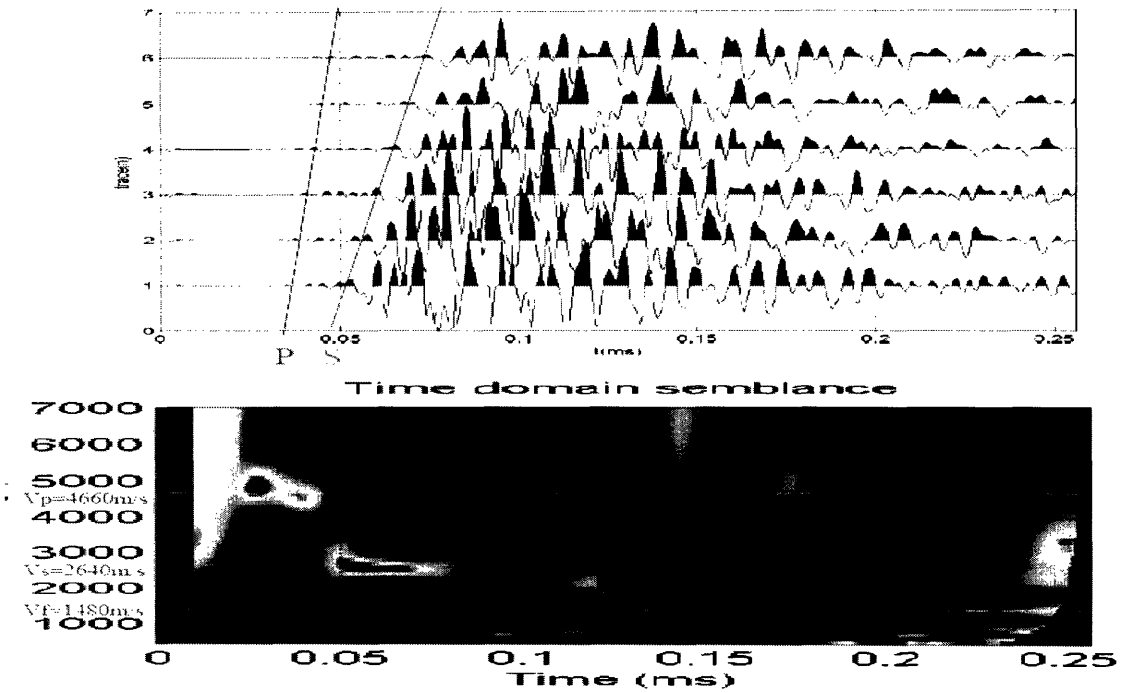

Fig 3.5 Monopole acoustic waveforms and their time domain semblances when the tool works in a sandstone borehole without connector. (Vp stands for formation P wave velocity, Vs for formation S wave velocity, and Vf for fluid velocity; P means P wave, S means S wave.)

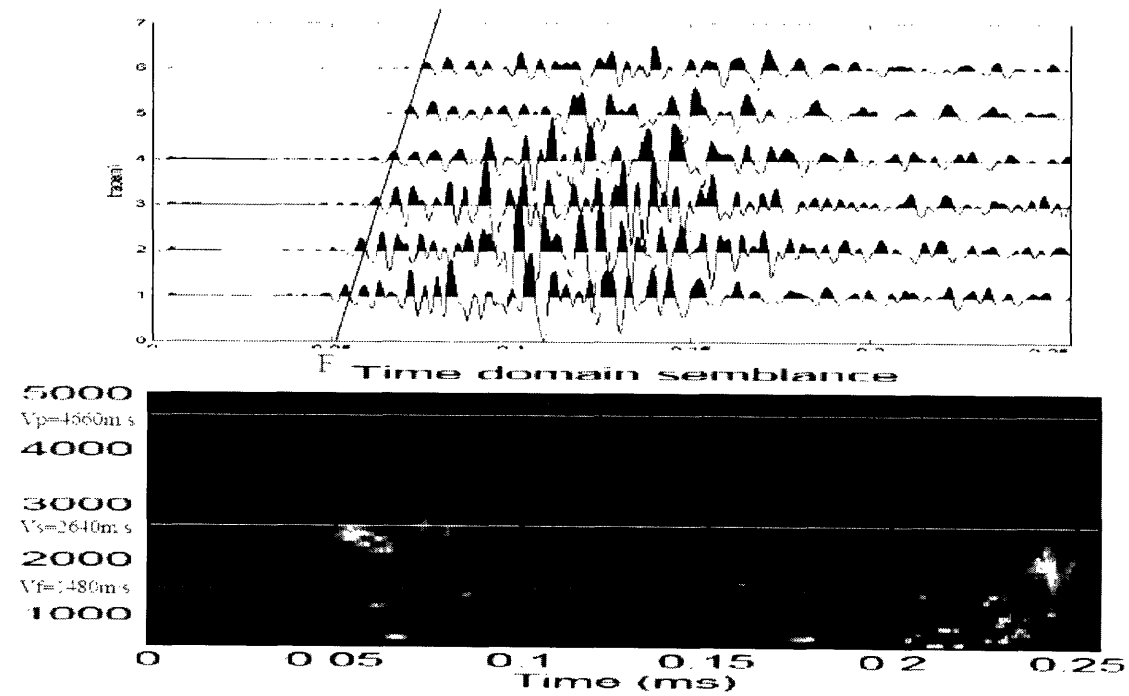

Fig 3.6 Dipole acoustic waveforms and their time, frequency domain semblances when the tool works in a sandstone borehole without connector. (Vp stands for formation P wave velocity, Vs for formation S wave velocity, and Vf for fluid velocity; F means formation flexural wave.)

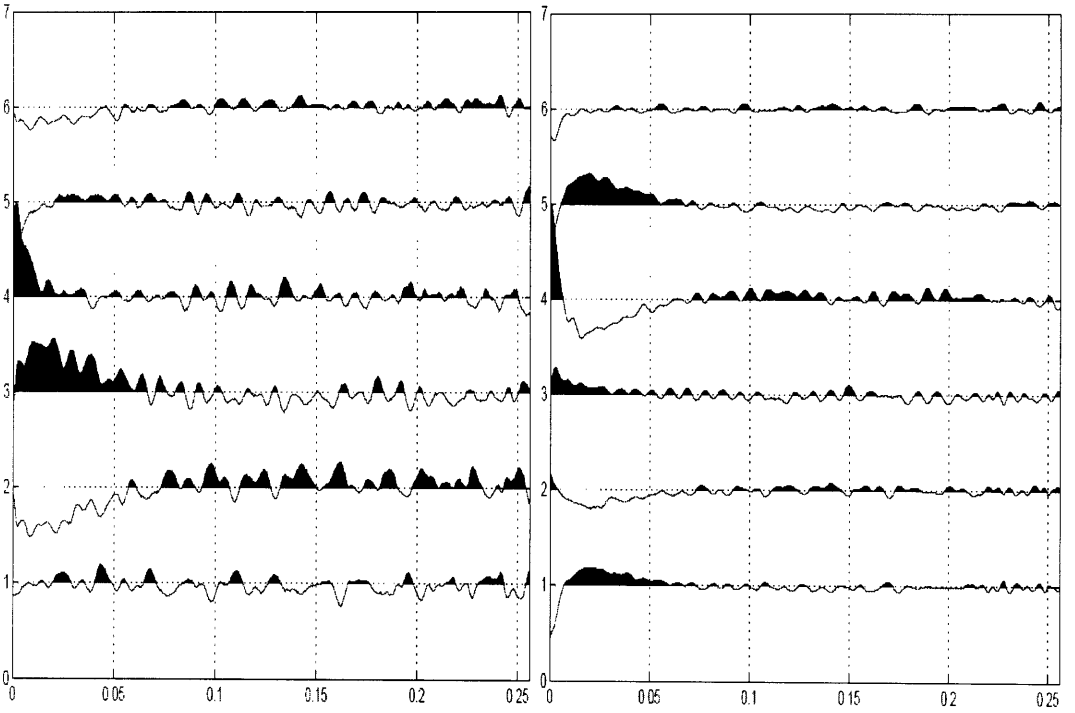

(A) (B)

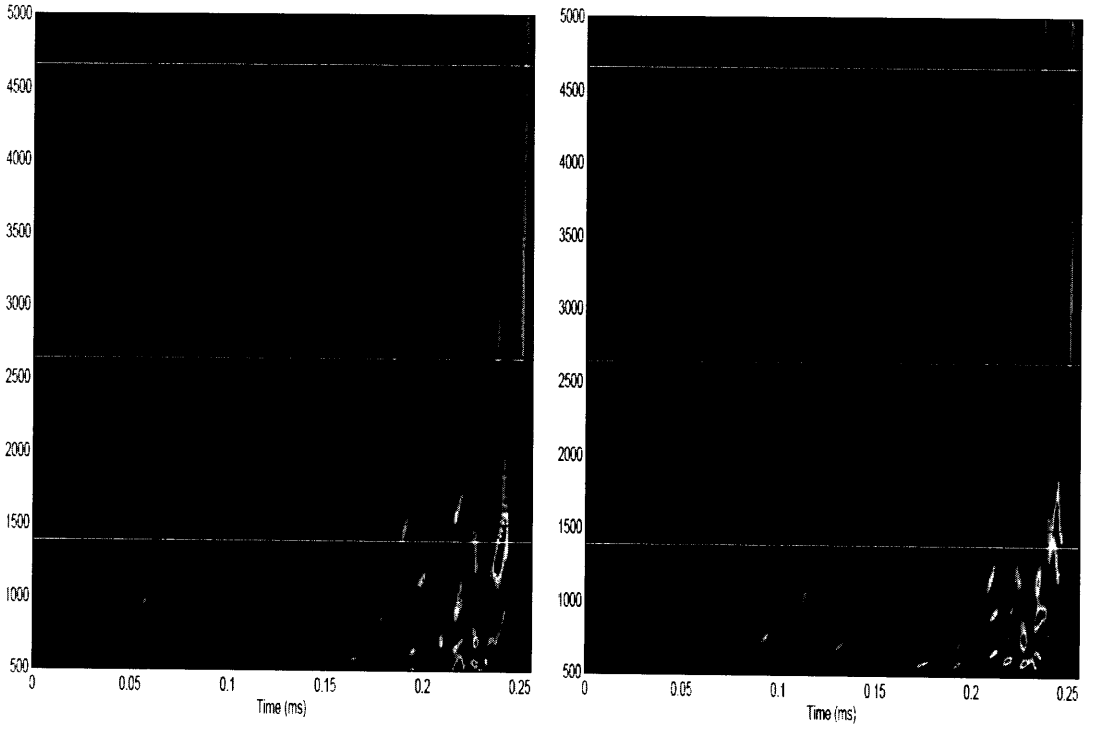

(C) (D)

Fig 3.7 Monopole (A) and Dipole (B) seismoelectric waveforms and their time domain semblance (C) and (D) at the steel-fluid interface

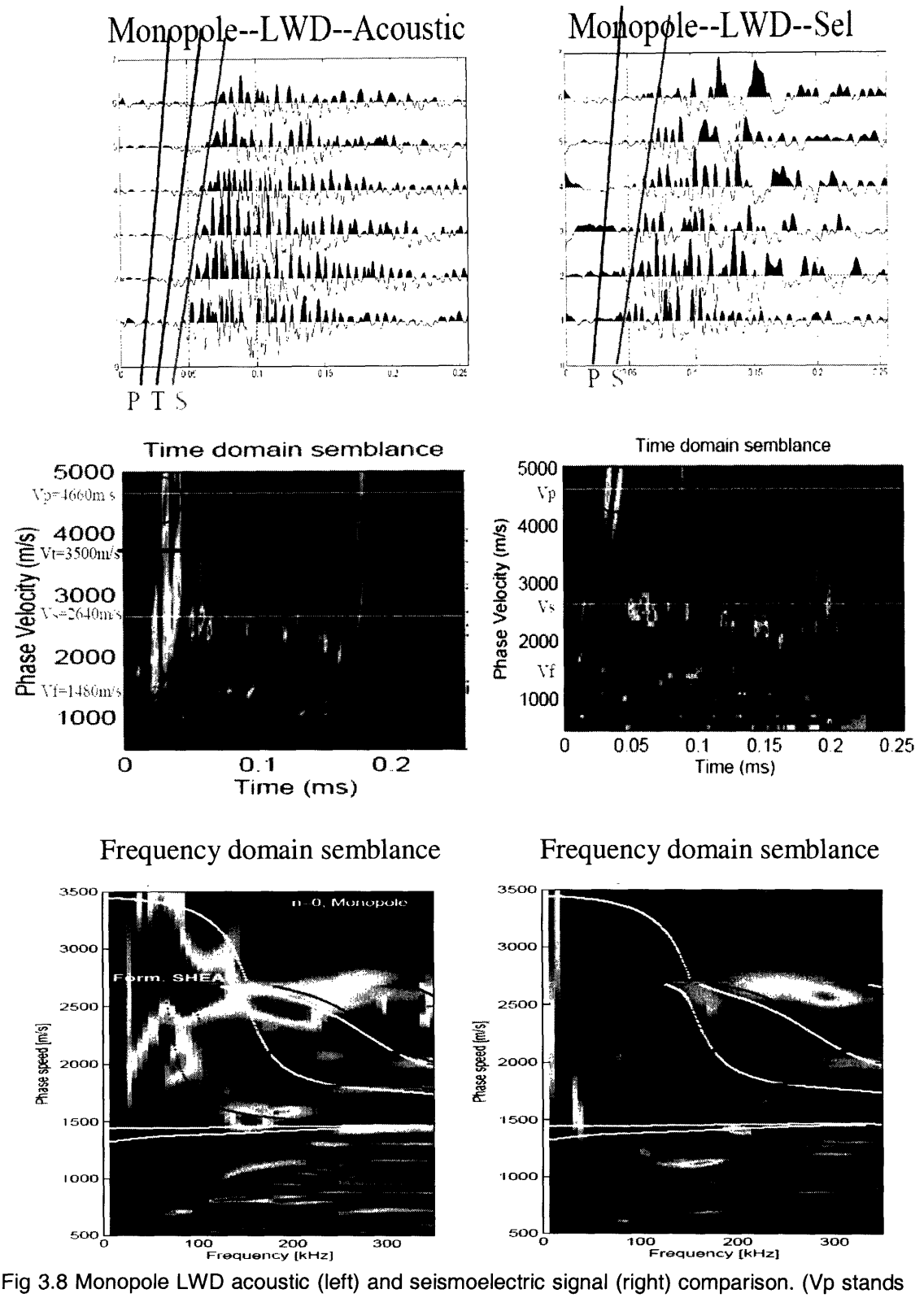

Fig 3.8 Monopole LWD acoustic (left) and seismoelectric signal (right) comparison. (Vp stands for formation P wave velocity, Vs for formation S wave velocity, and Vf for fluid velocity; P means P wave, S means S wave, T means tool wave. The superposed lines in frequency semblance correspond to the various monopole modes indicated in Chapter 2.)

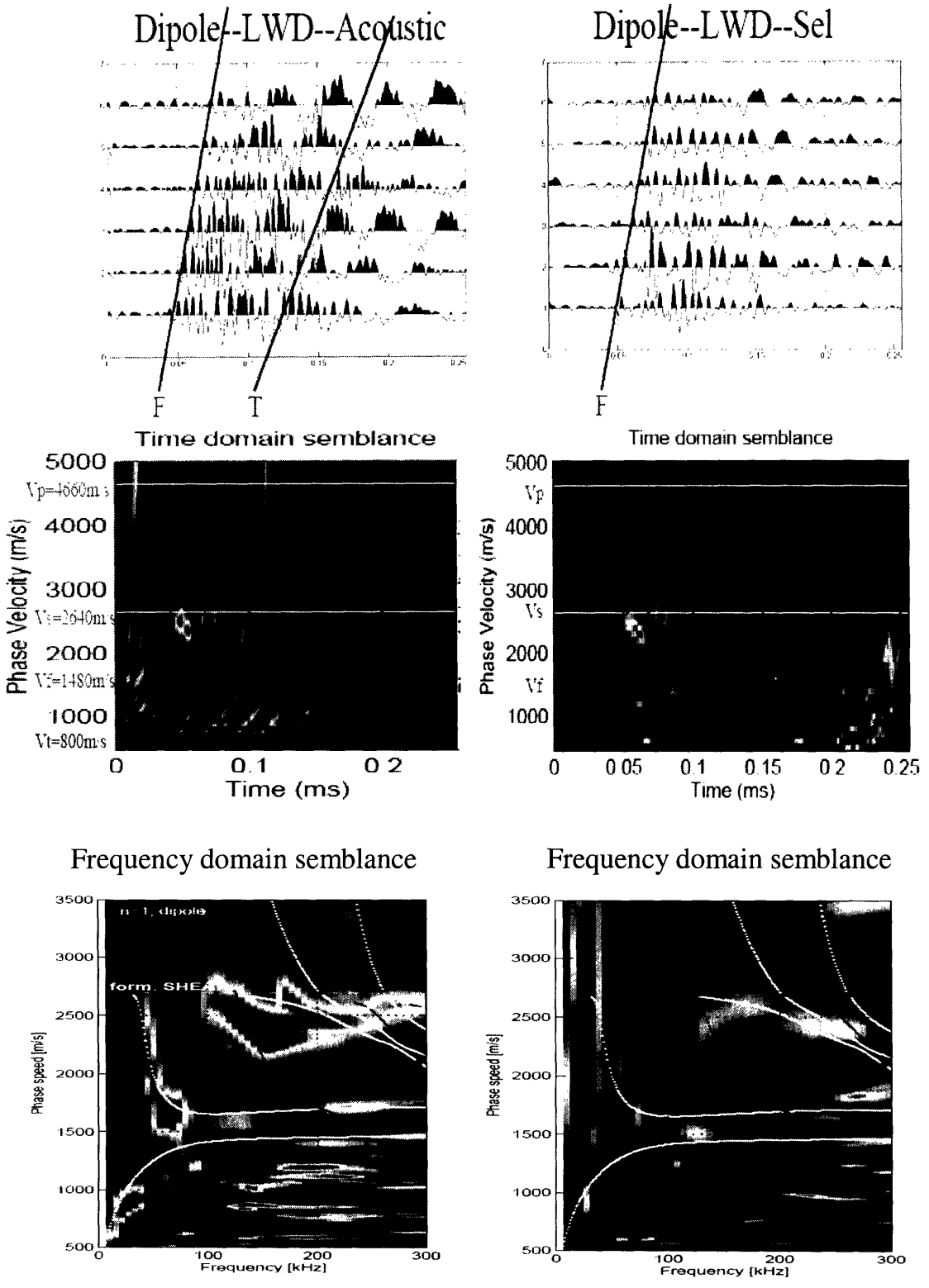

Fig 3.9 Dipole LWD acoustic (left) and seismoelectric signal (right) comparison. (Vp stands for formation P wave velocity, Vs for formation S wave velocity, and Vf for fluid velocity; F means formation flexure wave, T means tool wave. The superposed lines in frequency semblance correspond to the various monopole modes indicated in Chapter 2.)

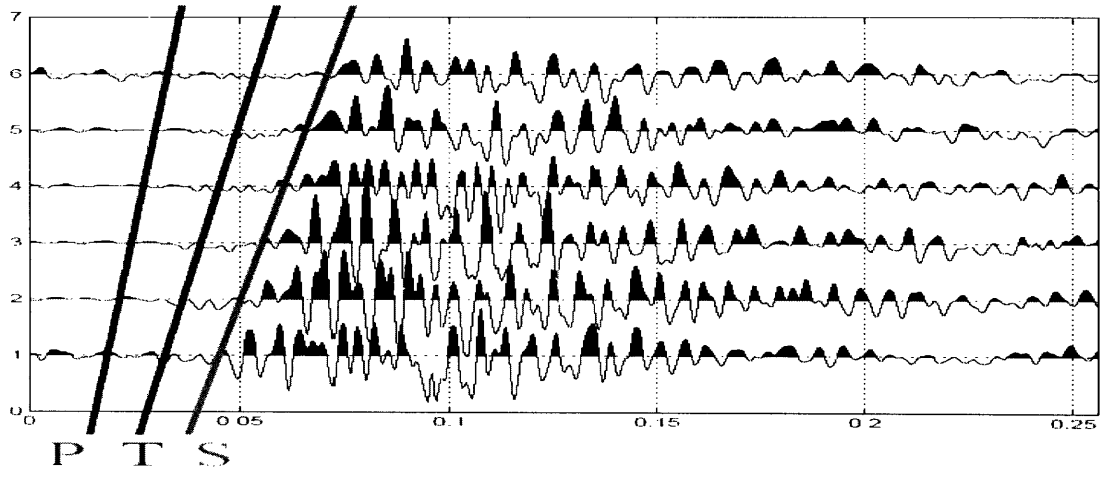

(a)

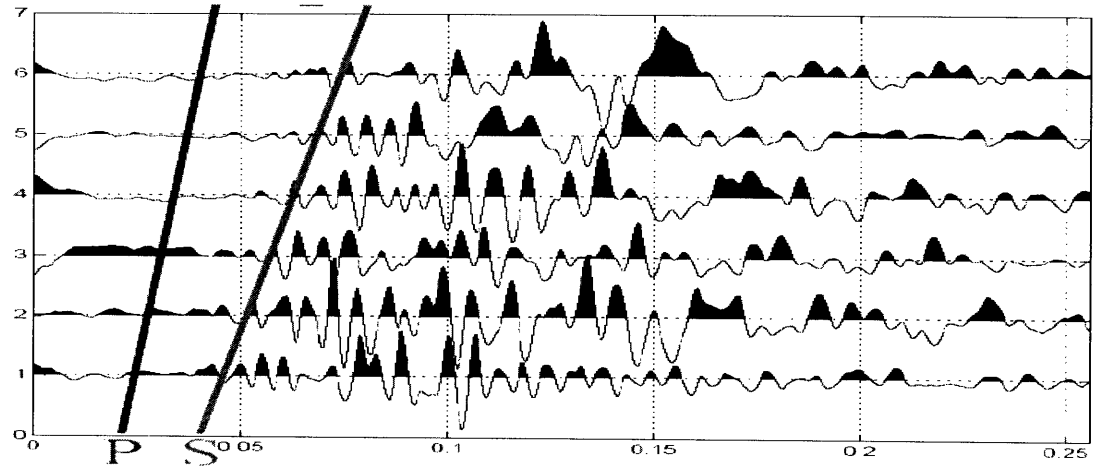

(b)

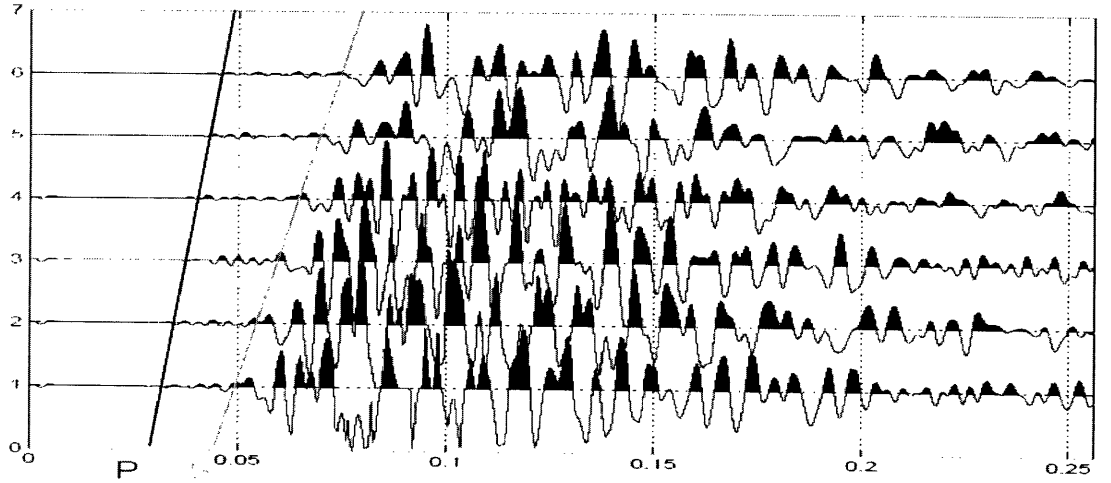

(c)

Fig 3.10 Monopole LWD acoustic (a) and seismoelectric signal (b) and acoustic signal taken when the tool works without connector (c) (P means P wave, S means S wave, T means tool wave).

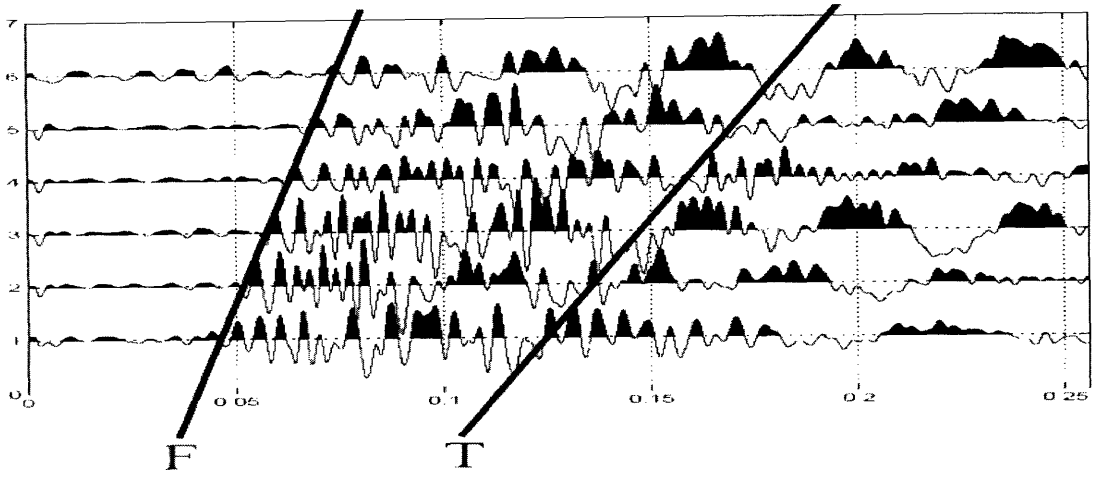

(a)

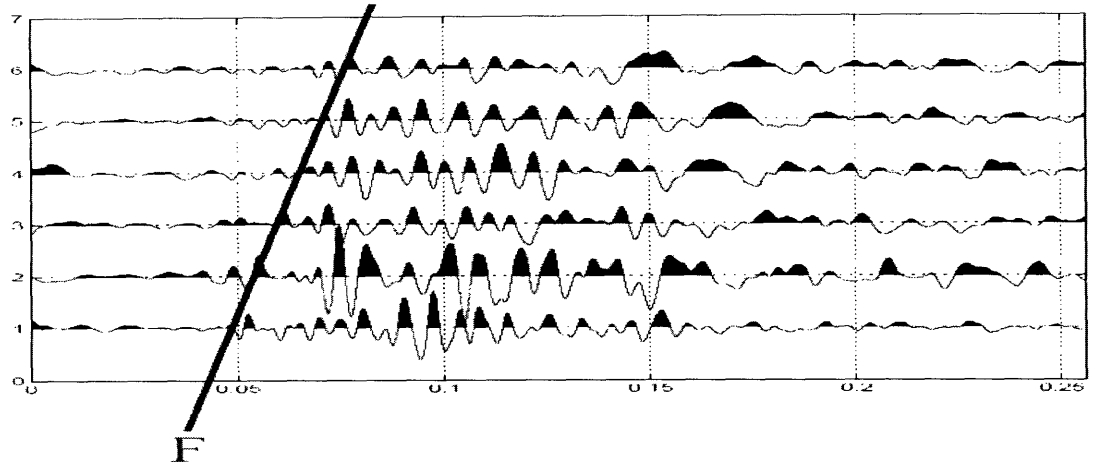

(b)

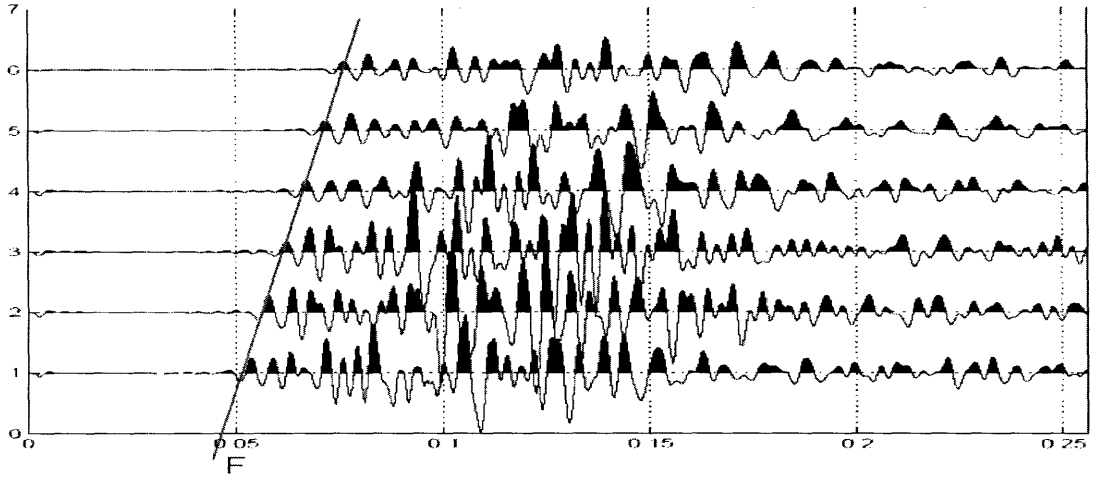

(c)

Fig 3.11 Dipole LWD acoustic (a) and seismoelectric signal (b) and acoustic signal taken when the tool works without connector (c) (F means formation flexural wave, T means tool wave).

even more complex. The seismoelectric signal in the LWD process, do not contain tool mode induced electric signals. Given that the LWD acoustic and seismoelectric (SE) signals are different in content, we can use the SE signal to filter the acoustic signal to eliminate the tool modes. The idea can be illustrated in Fig 3.12.

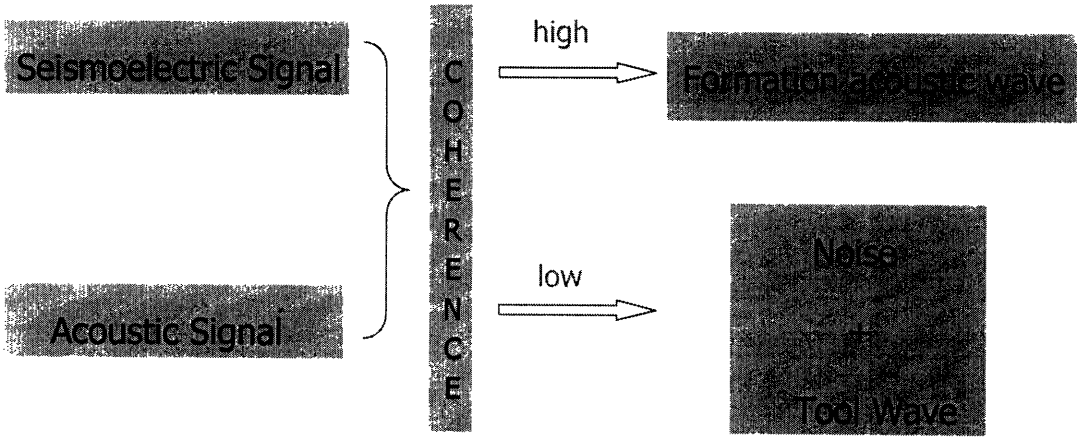

Fig 3.12 LWD acoustic and seismoelectric signal coherence

We calculate the correlation coefficient between the frequency spectra of the acoustic and SE signals to measure coherence. There are several reasons for this to be done in the frequency domain instead of the time domain. ① The time series can be decomposed into a finite number of frequency components. In the frequency range where the formation acoustic wave modes exist, the waveforms overlap better. In other frequency ranges where the waveforms differ greatly due to the different modes content, it is difficult to find the correlation between the two signals. ② There exists a phase shift of $\pi/2$ between acoustic and seismoelectric signals as predicted by the

governing equations for the coupled electromagnetics and acoustics of porous media (Pride, 1994, see from equation 4.4). ③ In the acoustic record, it takes time for the main acoustic energy to propagate from the borehole wall to the receiver transducer at the fluid acoustic velocity. While the propagation time for the electric signal can be ignored due to the high EM wave speed. Thus, it is more difficult to compare the two signals in time domain than in the frequency domain.

To find the coherence in frequency domain, we first apply the fast fourier transform (FFT) to calculate the spectra of the two signals, which is the average of the spectra of the six traces in both signals. We then calculate the correlation coefficients of the two frequency curves defined by

$$r = \frac{\sum_m (A_m - \bar{A})(B_m - \bar{B})}{\sqrt{\sum_m (A_m - \bar{A})^2 (B_m - \bar{B})^2}} \qquad (3.6)$$

where $\bar{A} = mean(A)$, $\bar{B} = mean(B)$, m is the index of the sampling point in frequency domain. A moving window is used to scan the spectra of the two signals simultaneously. The correlation coefficient of that window is set as the coherence value for the center frequency of the window. After obtaining a coherence curve (Fig 3.13 b, 3.14 b), we use it to design a zero-phase filter to be applied to the acoustic signal. A time domain semblance for the filtered data is then computed. We can see clearly that the filtered data contains only formation acoustic modes (Fig 3.13 c, 3.14 c). Other benefits of this filtering method include the reduction of noise in the acoustic signal as well. To further

demonstrate these benefits, we detect the peaks in the acoustic and seismoelectric signal spectra and calculate the corresponding wave velocity of those frequency peaks. We find that in the frequency range with low coherence the wave velocities are also different, which means the wave modes are different.

The coherence curves and the filtered results are shown in Fig 3.13 for monopole excitation and Fig 3.14 for dipole excitation. In Fig 3.13, ST stands for Stoneley wave, T stands for monopole tool wave. In Fig 3.14, F stands for dipole flexural wave, T stands for dipole tool wave. The monopole coherence curve is similar to a high pass filter, which is consistent with the fact that monopole tool wave exists in the low frequency range as indicated in Chapter 2. The dipole coherence curve is similar to a band pass filter.

The above analysis illustrates that by correlating the LWD seismoelectric signal with the acoustic signal, we can pick out formation acoustic modes from the LWD acoustic measurement and reduce the noise. This is a very significant result for extracting the formation arrivals from real-time LWD field data that may be contaminated by noise from drilling, mud circulation as well as the complex tool modes.

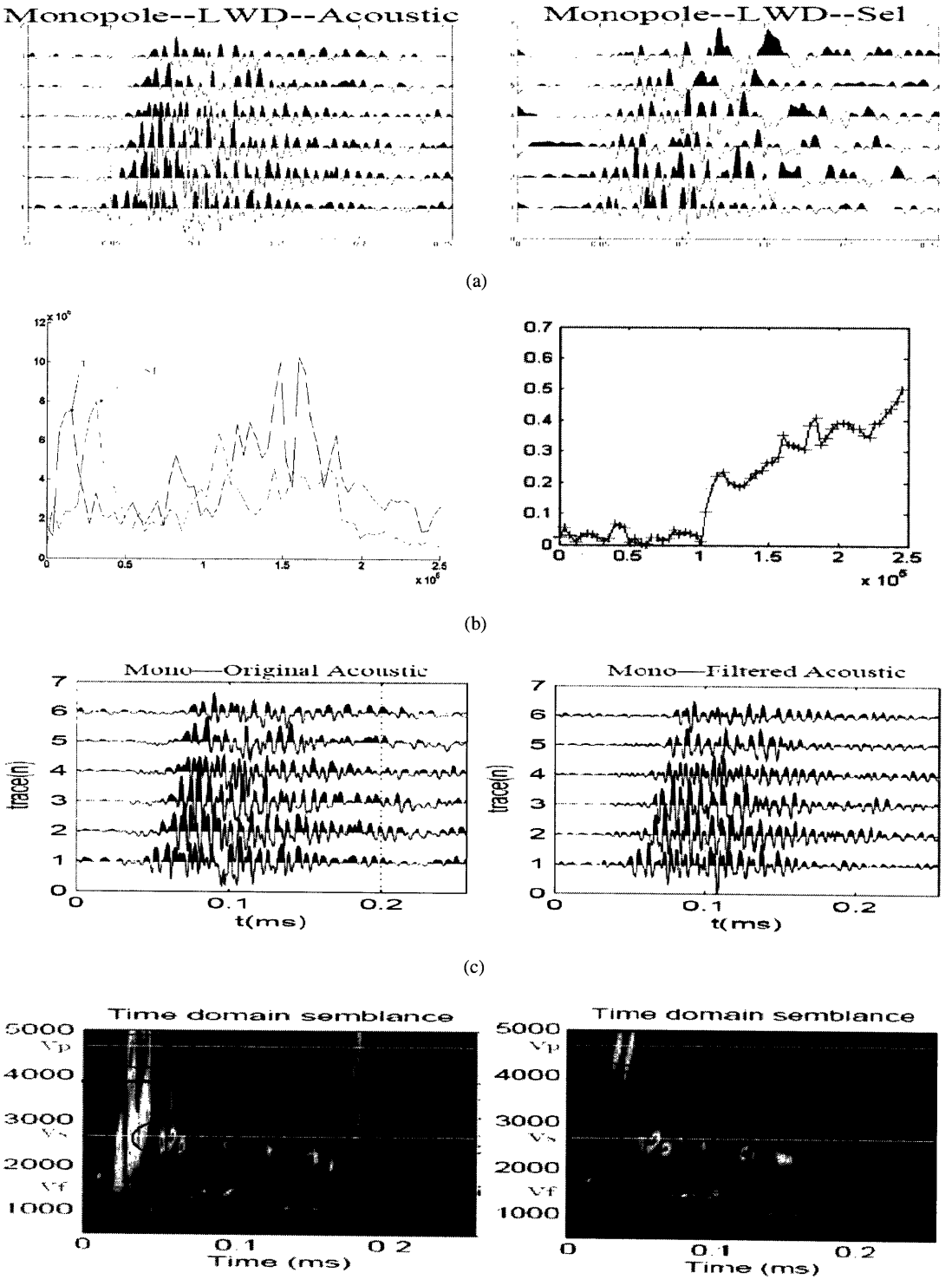

Figure 3.13 (a) Monopole acoustic (left) and seismoelectric (right) waveforms; (b) monopole acoustic (line with arrow "T") and seismoelectric (line with arrow "ST"). Fourier amplitude spectra (left) and coherence as a function of frequencies (right); (c) monopole unfiltered acoustic (left) and filtered (right) waveforms; and (d) their time domain semblances. (T means frequency peak due to tool wave, ST stands for Stoneley wave).

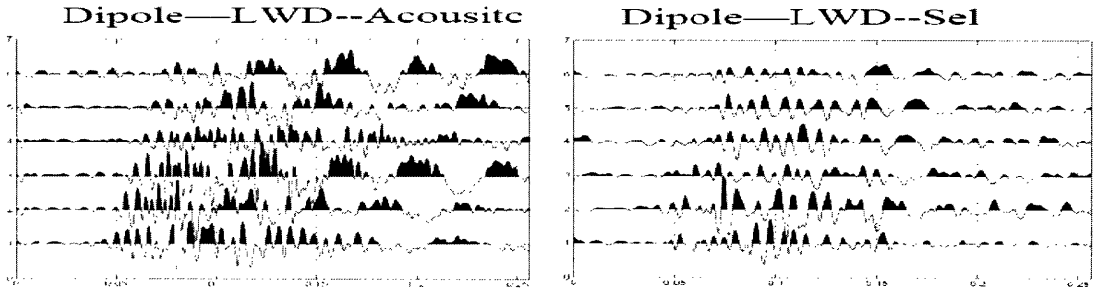

(a)

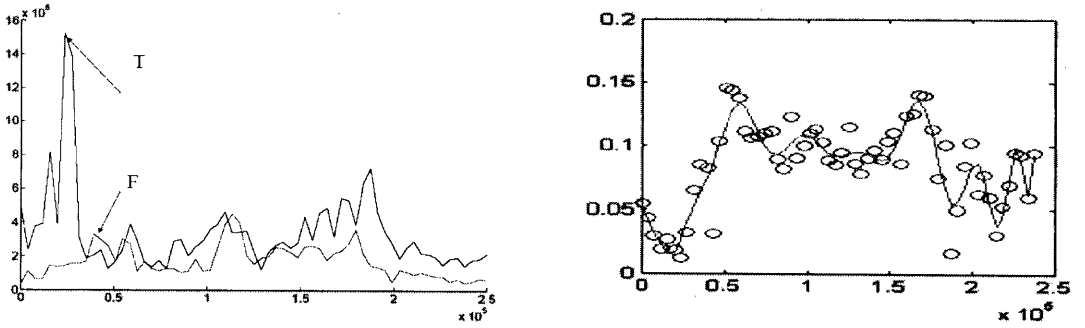

(b)

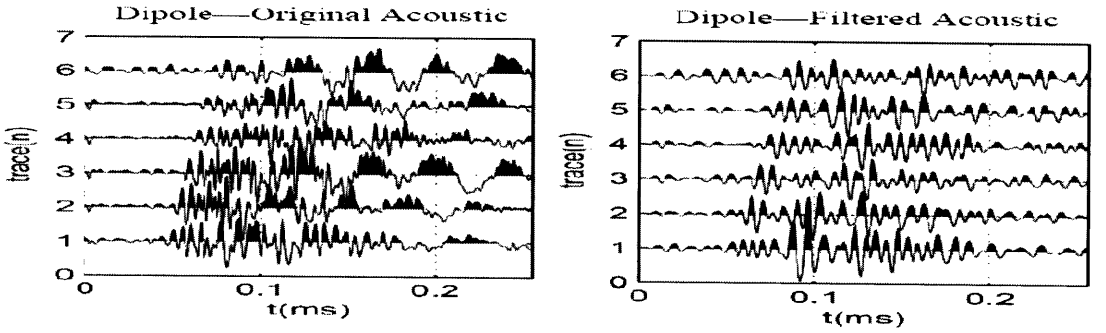

(c)

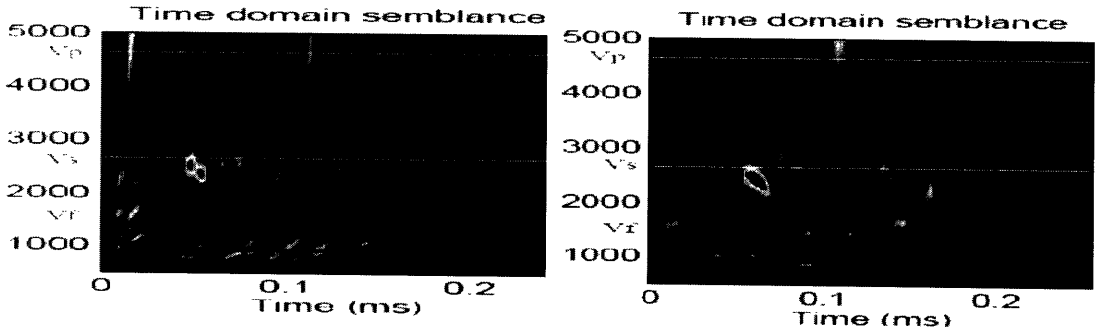

(d)

Figure 3.14 (a) Dipole acoustic (left) and seismoelectric (right) waveforms; (b) dipole acoustic (line with arrow "T") and seismoelectric (line with arrow "F") Fourier amplitude spectra (left) and coherence as a function of frequencies (right); (c) dipole unfiltered acoustic (left) and filtered (right) waveforms; and (d) their time domain semblances. (T means frequency peak due to tool wave, F stands for Flexural wave).

Chapter 4

Theoretical modeling of the LWD seismoelectric signal

In this chapter, we apply the Pride's governing equations into the LWD geometry to develop a theoretical model for the LWD-acoustic-wave induced electric field. Both the acoustic pressure and the electric field strength are calculated by matching the acoustic and electric boundary conditions at the three boundaries in our LWD model. The synthetic acoustic and electric waveforms calculated in a slow formation under the dipole excitation clearly demonstrate the absence of the dipole tool modes. It also helps us to understand the relationship between the acoustic pressure and the converted electric field strength as given out in Pride's equations. Finally, we carry out numerical calculations for our laboratory measurements, described in Chapter 3, in order to compare the experimental and theoretical results. A consistent conclusion, which is the absence of the tool modes in the LWD seismoelectric signals, can be drawn in both experimental and theoretical results.

4.1 LWD-acoustic-wave induced electric field along the borehole in a homogenous, elastic formation

In this section we develop a theoretical model to simulate the seismoelectric effect during the LWD process in a borehole. The modeling was performed for an isotropic, homogenous elastic formation and both axially symmetric (monopole) and axially non-symmetric (dipole) sources.

4.1.1 Modeling the acoustic wave propagation in logging-while-drilling

The presence of a logging tool in the borehole will modify the excitation and propagation characteristics of the borehole acoustic waves (Tang et al., 2002; Huang, 2003). To model the acoustic wave propagation in the logging-while-drilling (LWD) configuration, we use the acoustic theory for a multi-layered system. The tool body is made of steel, its elastic moduli and density are much higher than those of the borehole fluid. The dimension of the source on the acoustic tool cannot be ignored, thus we use an acoustic ring source instead of point source in the LWD modeling.

The geometry of the borehole and the logging tool is shown in Fig 4.1. The axial direction is z; radial direction is r. The borehole formation is a homogenous, elastic formation. The acoustic logging tool is modeled as a cylindrical structure with the outer radius (tool OD) r_2, a multipole ring source is constructed by a distribution of the point sources along the tool rim.

Both the source and receivers are located at the tool outer radius where $r_{source} = r_{receiver} = r_2$. By summing the contributions of all these point sources, the resulting radial displacement at the source location can be expressed in the wave-number domain as (Tang and Cheng, 2004)

$$u = \varepsilon_n(-nK_{n-1}(fr_2)/r_2 - fK_n(fr_2))I_n(fr_2)\cos(n(\theta-\phi)). \qquad (4.1)$$

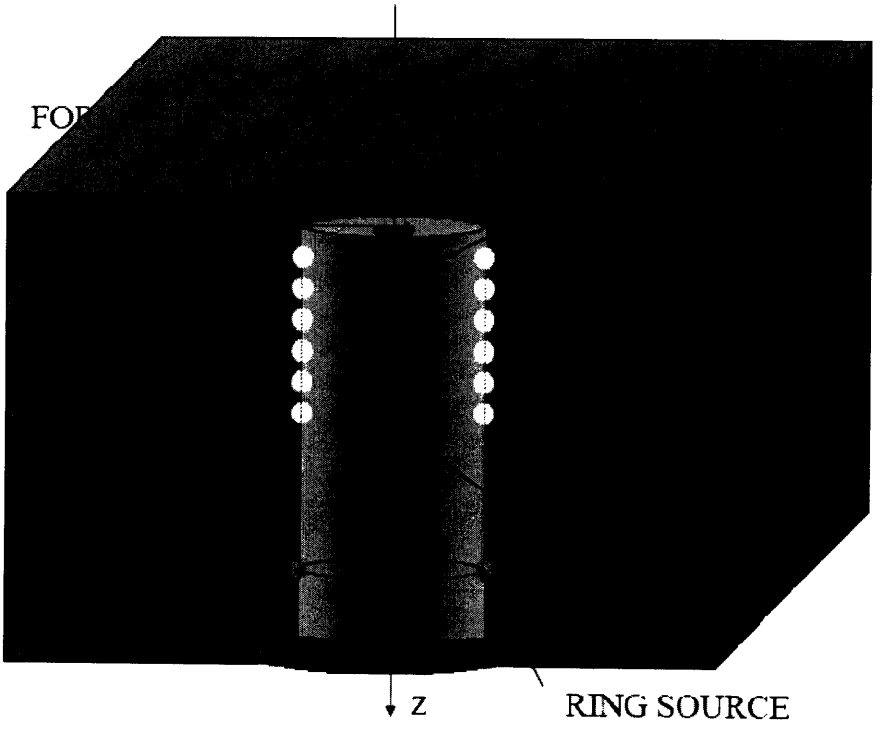

Fig 4.1 Geometry of the borehole and logging tool in the modeling. (r_1, r_2, r_3 indicates the inner fluid , tool outer layer and borehole radius respectively.)

Here, ε_n is 1 for $n=0$, and 2 for $n>0$ where n is the azimuthal order number with $n=0,1,2$ corresponding to monopole, dipole and quadrupole source, respectively. I_n and $K_n(n=0,1,\ldots)$ are the modified Bessel functions of the first and second kind of order n. $f=(k^2-k_f^2)^{1/2}$ is the radial

wavenumber, where k is the axial wavenumber and $k_f = \omega/\alpha_f$; ω is the angular frequency and α_f is the fluid acoustic velocity. The cylindrical coordinate (r,θ,z) is used and ϕ is a reference angle to which those point source location are referred.

Finally, we apply the acoustic boundary conditions (see detail in Appendix A) to the three boundaries (inner fluid tool inner layer, tool outer layer outer fluid, outer fluid borehole wall) and a Ricker wavelet of the form (Aki and Richards, 1980)

$$S(\omega) = \left(\frac{\omega}{\omega_0}\right)^2 e^{i\left(\omega/\omega_0\right)^2} \tag{4.2}$$

to calculate the pressure waveform at the rim of the tool.

4.1.2 The converted electric field along a borehole wall

When a fluid electrolyte comes into contact with a solid surface (such as our borehole wall), anions from solution absorb to the solid surface leaving a diffuse distribution of excess cations in a region of near the wall. This region is known as the electric double layer (Pride and Morgan, 199; Bockris and Reddy, 2000). When a pressure gradient is applied to the tube surface (borehole wall), the excess charge in the double layer carried along by the fluid flow will give rise to a streaming electric current (Mikhailov, 1998, 2000; Zhu et al., 1999). The streaming current produces an electric field. In turn, this electric field drives a conductive electric current in opposition to the streaming current. The

total electric current density is the sum of the streaming current and the conduction current.

According to Pride's theory (1994, Appendix B; Pride and Haartsen, 1996), the elastic field is coupled with the electromagnetic field. The coupling between the acoustic and electromagnetic field in a porous media can be expressed by

$$J = \sigma E + L(-\nabla p + \omega^2 \rho_f u) \tag{4.3}$$

$$-i\omega w = LE + (-\nabla p + \omega^2 \rho_f u)\kappa/\eta, \tag{4.4}$$

where, J is the total electric current density, E is the electric field strength, u is the solid frame displacement, w is the fluid filtration displacement and p is the pore fluid pressure. L is the coupling coefficient, ρ_f and η are the density and the viscosity of the pore fluid, κ and σ are the dynamic permeability and conductivity of the porous medium respectively, ω is the angular frequency. The detailed expressions of L, κ are given in Appendix C derived by Pride (1994). In our numerical simulation, the L value is calculated by using a porous formation with the medium parameters listed in the table C.1 in Appendix C.

Under the assumption that the influence of the converted electric field on the propagation of the elastic waves can be ignored (Hu et al., 2000; Hu and Liu, 2002; Chi et al., 2005), we can further reduce the equation (4.4) to

$$-i\omega w = (-\nabla p + \omega^2 \rho_f u)\kappa/\eta \tag{4.5}$$

We can express the electric field as the gradient of the electric potential

$$E = -\nabla\phi. \tag{4.6}$$

Taking the divergence of equation (4.1) and using equation (4.6) with the generalized Ampere's law, we can have

$$J = \sigma E + L(-\nabla p + \omega^2 \rho_f \nabla \cdot u) \tag{4.7}$$

Since $\nabla \cdot u = \nabla^2 \varphi$, where φ is the displacement potential of the gradient field, equation (4.7) can be written as

$$\nabla^2 \phi = (L/\sigma)(-\nabla^2 p + \omega^2 \rho_f \nabla^2 \varphi). \tag{4.8}$$

To solve the equation (4.8) in the wavenumber domain, we get

$$\phi = A \cdot K_n(kr) + (L/\sigma)(-p + \omega^2 \rho_f \varphi) \tag{4.9}$$

where k is the axial wavenumber, $Kn(kr)$ is the modified Bessel function of nth order and A is the unknown coefficient for the electric field to be decided by the electric boundary conditions.

When the formation is homogenous and elastic, we can deduce the relationship between the coupled acoustic field potential and the electric field potential by deleting the pore pressure term in equation (4.9) and get

$$\phi = A \cdot K_n(kr) + (L/\sigma)\omega^2 \rho_f \varphi. \tag{4.10}$$

4.1.3 The converted electric field along the elastic borehole wall and in the borehole with the LWD geometry

In the LWD geometry, using the expression of the displacement potentials in the elastic formation which is the $4th$ layer as indicated in the appendix A can be expressed as:

$$\begin{aligned} \phi_4 &= B_4 K_n(kp_4 r) \\ \chi_4 &= D_4 K_n(ks_4 r) \\ \Gamma_4 &= F_4 K_n(ks_4 r) \end{aligned} \tag{4.11}$$

and the displacement potential ϕ_4 is the φ in equation (4.8), (4.9) and (4.10).

In terms of potentials, the radial displacement component u_r in the elastic formation can be expressed as:

$$u_r = \frac{\partial \phi_4}{\partial r} + \frac{1}{r}\frac{\partial \chi_4}{\partial \theta} + \frac{\partial^2 \Gamma_4}{\partial r \partial z}. \tag{4.12}$$

Combing the (4.11) and (4.12), we can get

$$u_r = B_4 K_n'(kp_4 r) + \frac{n}{r} D_4 K_n(ks_4 r) + iks_4 F_4 K_n'(ks_4 r). \tag{4.13}$$

Substituting (4.11) into (4.10) and (4.13) into (4.7), using the relationship in (4.6), we can get the expression for the potential ϕ_{wall}, radial strength $E_{r\,wall}$ and the streaming current density J_{wall} of electric field along the elastic borehole wall

$$\begin{aligned} \phi_{wall} &= AK_n(kr) + (L/\sigma)\omega^2 \rho_f B_4 K_n(kp_4 r) \\ E_{rwall} &= \frac{-\partial \phi_{wall}}{\partial r} = -AK_n'(kr) - (L/\sigma)\omega^2 \rho_f B_4 K_n'(kp_4 r) \\ J_{wall} &= -\sigma A K_n'(kr) + L\omega^2 \rho_f \left[\frac{n}{r} D_4 K_n(ks_4 r) + iks_4 F_4 K_n'(ks_4 r) \right] \end{aligned} \tag{4.14}$$

Under the quasi-static assumption, the electric field in the borehole satisfies the Laplace's equation (Hu and Liu, 2002), the solution for the potential ϕ_{flul}, radial strength $E_{r\,flu}$ and the streaming current density J_{flu} is

$$\begin{aligned}
\phi_{flu} &= BI_n(kr) + CK_n(kr) \\
E_{rflu} &= \frac{-\partial \phi_{flu}}{\partial r} = -BI_n'(kr) - CK_n'(kr) \\
J_{flu} &= -\sigma \frac{\partial \phi_{flu}}{\partial r} = -\sigma\left[BI_n'(kr) + CK_n'(kr)\right]
\end{aligned} \tag{4.15}$$

where B and C are the coefficients to be decided by the electric boundary conditions as well.

4.1.4 Electric boundary conditions in the LWD seismoelectric conversion

To solve the three coefficients A, B and C in the above expressions for the converted electric fields along the borehole wall (equation (4.14)) and in the borehole fluid (equation (4.15)), we apply the following three boundary conditions. On the borehole wall where $r = r_3$, we have

$$\begin{aligned}
\phi_{wall} &= \phi_{flu} \\
J_{wall} &= J_{flu}
\end{aligned} . \tag{4.16}$$

At the tool surface where $r = r_2$, we use the condition that the radial current density or the radial electric field strength (since they only differ in the multiplication of a conductivity) is equal to zero

$$E_{flu}(r_2) = 0 . \tag{4.17}$$

Substituting equation (4.14) and (4.15) into the three boundary conditions, we could rewrite the boundary conditions in the matrix formation as following

$$\begin{bmatrix} \frac{-I_n'(kr_2)}{K_n'(kr_2)}K_n(kr)+I_n(kr) & -K_n(kr) \\ \frac{-I_n'(kr_2)}{K_n'(kr_2)}K_n'(kr)+I_n'(kr) & -K_n'(kr) \end{bmatrix} \begin{bmatrix} B \\ A \end{bmatrix} = \begin{bmatrix} (L/\sigma)\omega^2\rho_f B_4 K_n(kp_4 r) \\ -(L/\sigma)\omega^2\rho_f \left[\frac{n}{r} D_4 K_n(ks_4 r) + iks_4 F_4 K_n'(ks_4 r) \right] \end{bmatrix}$$

. (4.18)

From equation (4.18), we could get A and B after we solve the acoustic coefficients B_4, D_4 and F_4 by applying the LWD acoustic boundary conditions as indicated in Appendix A. Electric coefficient C can be calculated by substituting B into equation (4.17). Once A, B and C are all determined, the electric field both along the borehole wall and within the borehole fluid can be determined.

4.2 The synthetic waveforms of the LWD acoustic and seismoelectric signal

The synthetic waveforms for the monopole, dipole acoustic and seismoelectric signals are calculated in both fast and slow formation in this section. For the acoustic waveforms, we calculate the acoustic pressure on the rim of the logging tool. For the electric signal, we calculate the electric field strength at the borehole wall. As we measure in the laboratory experiment, we use the acoustic transducer imbedded in the tool surface to record the acoustic pressure at the tool rim. The electrodes protruding from the tool surface, very close to the borehole wall, measure the converted electric field strength at the borehole wall.

4.2.1 The borehole geometry and medium parameters in the modeling

To further compare the theoretical model results with the lab experiment measurements, the borehole geometry parameters we use are scaled to the lab borehole. The formation properties are the same as the lab formation. The four layer model we use to simulate the LWD process is listed in the table 4.1. A scaling factor of 17 is used to scale the lab tool to the real LWD tool. The source wavelet in the experiment is a square wave with a center frequency of 100 kHz. Scaling the 100kHz center frequency to the modeling, we use a Ricker wavelet with the center frequency of 6kHz as a source. The formulae in both acoustic and electric calculations are expressed in the wavenumber domain, thus we use the discrete wavenumber method (Bouchon and Schimitt, 1989; Bouchon, 2003) to do the modeling.

4.2.2 Synthetic acoustic and electric waveform comparison

Figure 4.2 shows the calculated monopole waveforms of the acoustic pressure at the tool rim and the converted electric field along the borehole wall in the slow formation described in the table 4.1. The center frequency of the source wavelet is 6kHz. The acoustic waveforms (plotted in the solid curves) and the electric waveforms (plotted in the dotted curves) in figure 4.2 at six different receiving locations are normalized to the largest amplitude of the acoustic and electric waveforms at the $1st$ trace respectively. The figures are

scaled back to the lab borehole tool scale with the first trace located at $z = 0.098$ m and the spacing is 0.012 m as shown in fig 2.4.

The radiating electromagnetic (EM) wave (A-A) arrives at each receiver simultaneously due to the high electromagnetic wave velocity. (B-B) is the dipole tool wave, which arrives second. (C-C) and (D-D) are formation compressional wave and formation flexural wave respectively. Each acoustic mode has a corresponding converted electric field, except the dipole tool wave (B-B). This can be observed more clearly in figure 4.3 which is an expanded time scale version of the wavetrain in figure 4.2. To further prove the relationship between acoustic pressure and the converted electric field strength as shown in equation (4.4), we compare the time derivative of the acoustic signal (solid curves in figure 4.4) and electric signal (dotted curves in figure 4.4). Figure 4.5 is the enlarged view of the first half part of the three traces which is indicated by the window in figure 4.4. A perfect match between the time derivative of the acoustic signal and the electric signal can be found in both figures.

4.2.3 Consistency of the theoretical model with the laboratory measurements

Figure 4.6 and figure 4.7 shows the calculated monopole and dipole waveforms using the fast formation parameters of our lab experiment. Solid

curves are the acoustic signals and the dotted curves are the electric signals. (A-A) is the radiating electromagnetic wave in both figures.

In figure 4.6, (B-B) is the formation compressional wave, (C-C) is the monopole tool wave and (D-D) represents the formation shear wave, (E-E) is the Stoneley wave. We use the same semblance method to analyze the wave modes in the acoustic and electric waveforms as we did for the experiment data. The time domain semblances for the monopole acoustic and electric waveforms are shown in figure 4.8 and figure 4.9 respectively. The absence of the monopole tool mode which is indicated by the first big block in figure 4.8 can be observed very clearly in the semblance of the electric signal (figure 4.9).

The same phenomena can be observed for the dipole case. In figure 4.7, (B-B), (C-C), (D-D) are the 1^{st} order dipole formation flexural wave, dipole tool wave and 2^{nd} order dipole formation flexural wave, respectively. The absence of the dipole tool mode, which is indicated by the second big block in figure 4.10, can be observed very clearly in the semblance of the electric signal (figure 4.11).

	P-velocity	S-velocity	Density	Outer radius
Inner fluid	$1500 m/s$	-------	$1000 kg/m^3$	0.024m
Tool (Composite)	$4185 m/s$	$2100 m/s$	$7700 kg/m^3$	0.085m
Outer fluid	$1500 m/s$	-------	$1000 kg/m^3$	0.11m
Fast Formation	$4660 m/s$	$2640 m/s$	$2100 kg/m^3$	∞
Slow Formation	$2000 m/s$	$1000 m/s$	$2100 kg/m^3$	∞

Table 4.1 LWD lab borehole model used in acoustic and seismoelectric modeling

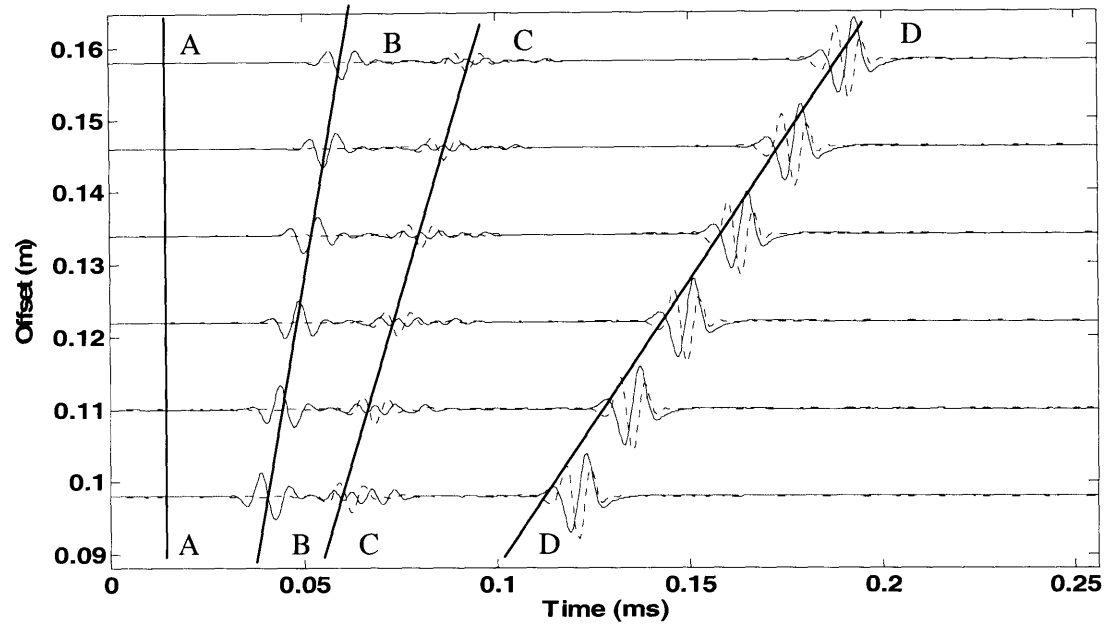

Fig 4.2 The dipole waveforms of the normalized acoustic pressure (solid curves) and the normalized electric field strength (dotted curves) for slow formation (A, B, C, D indicate the different arrivals described in the text).

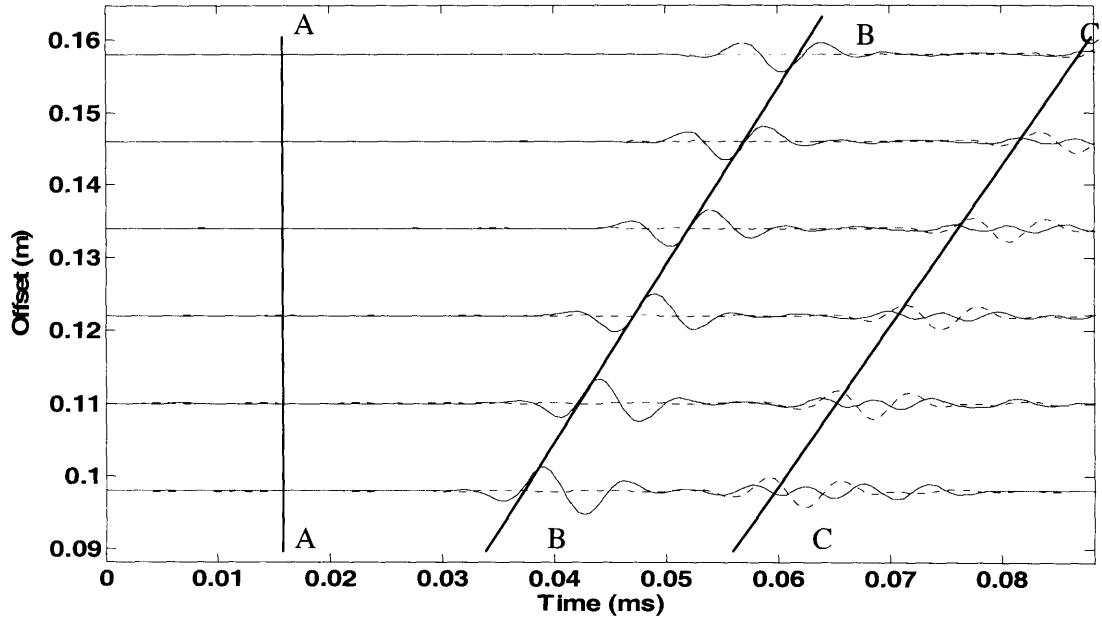

Fig 4.3 The first part of the dipole waveforms of the normalized acoustic pressure (solid curves) and the normalized electric field strength (dotted curves) for slow formation (A, B, C indicate the different arrivals described in the text)..

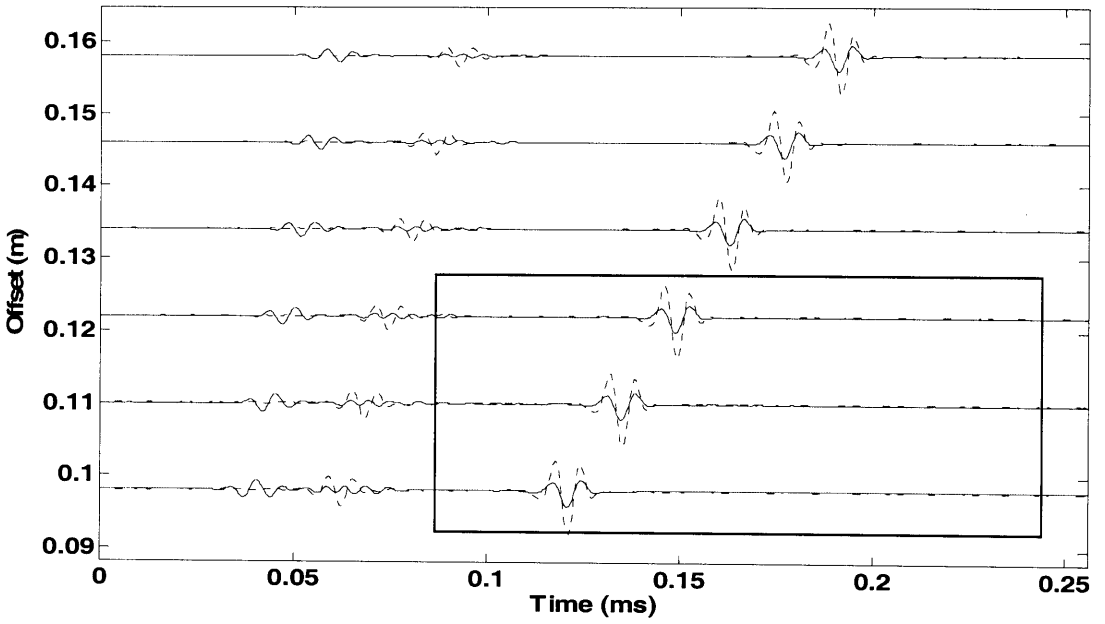

Fig 4.4 The dipole waveforms of the time derivative of the normalized acoustic pressure (solid curves) and the normalized electric field strength (dotted curves) for slow formation.

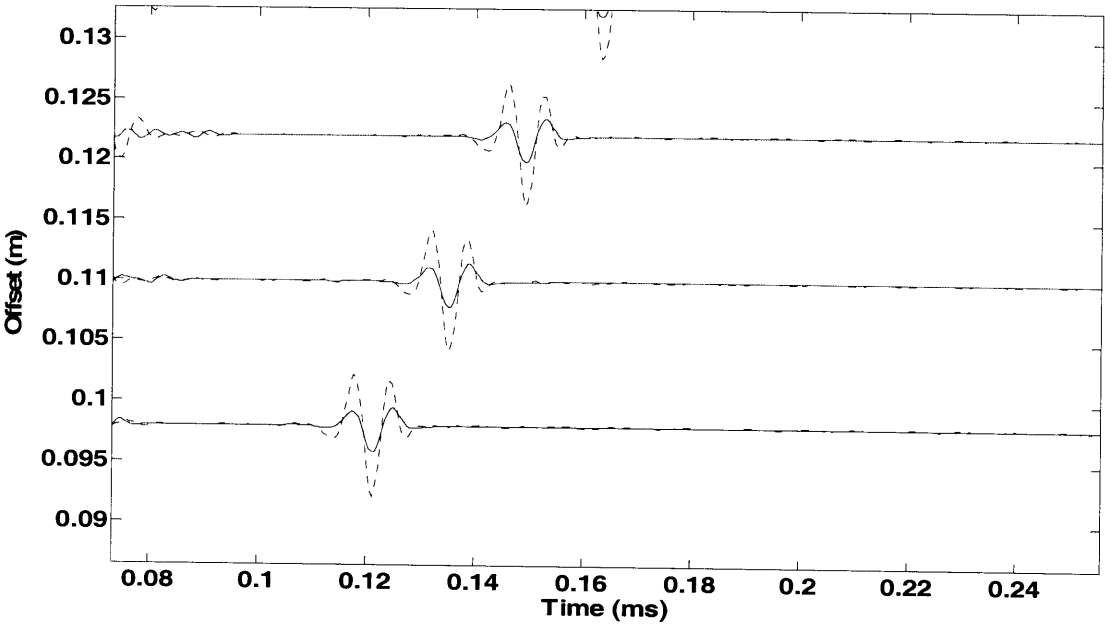

Fig 4.5 The enlarged view of the window in figure 4.4.

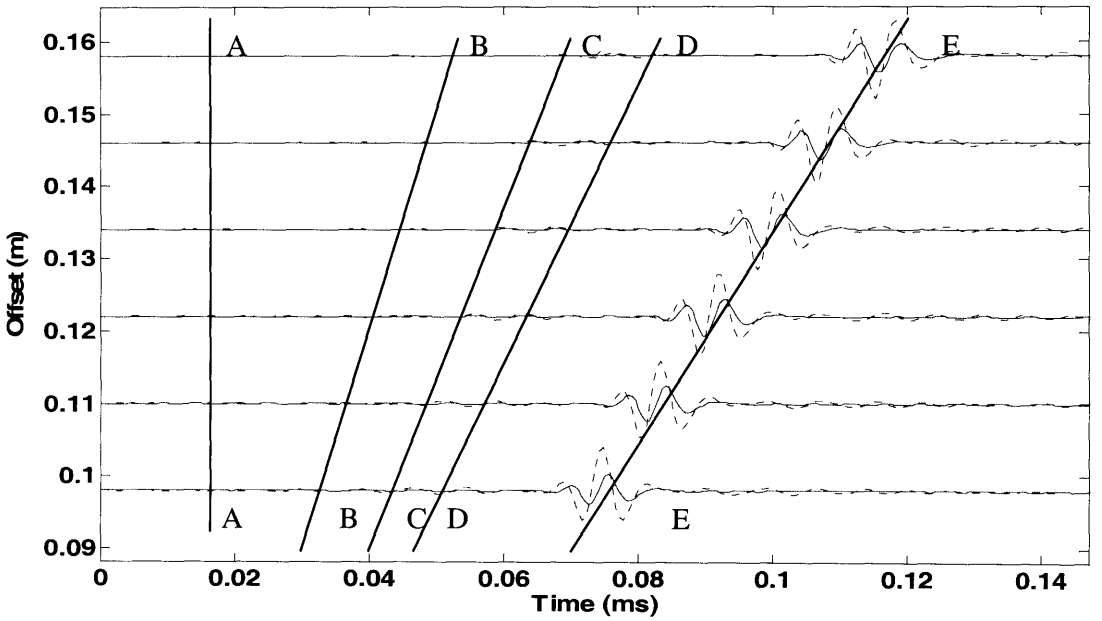

Fig 4.6 The monopole waveforms of the normalized acoustic pressure (solid curves) and the normalized electric field strength (dotted curves) for laboratory fast formation (A, B, C, D, E indicate the different arrivals described in the text).

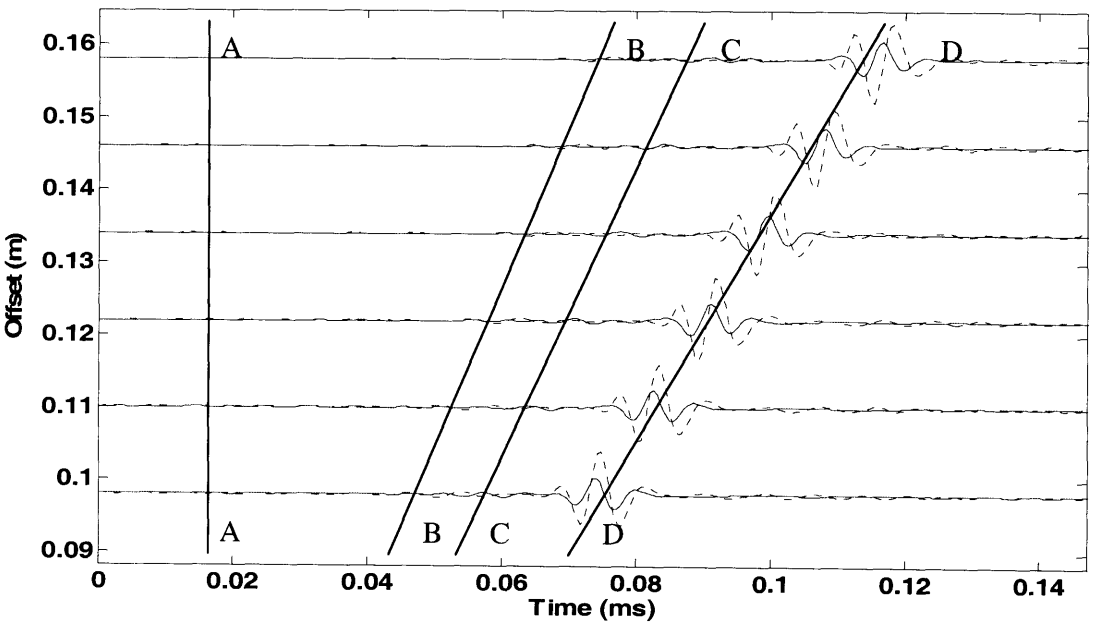

Fig 4.7 The dipole waveforms of the normalized acoustic pressure (solid curves) and the normalized electric field strength (dotted curves) for laboratory fast formation (A, B, C, D indicate the different arrivals described in the text).

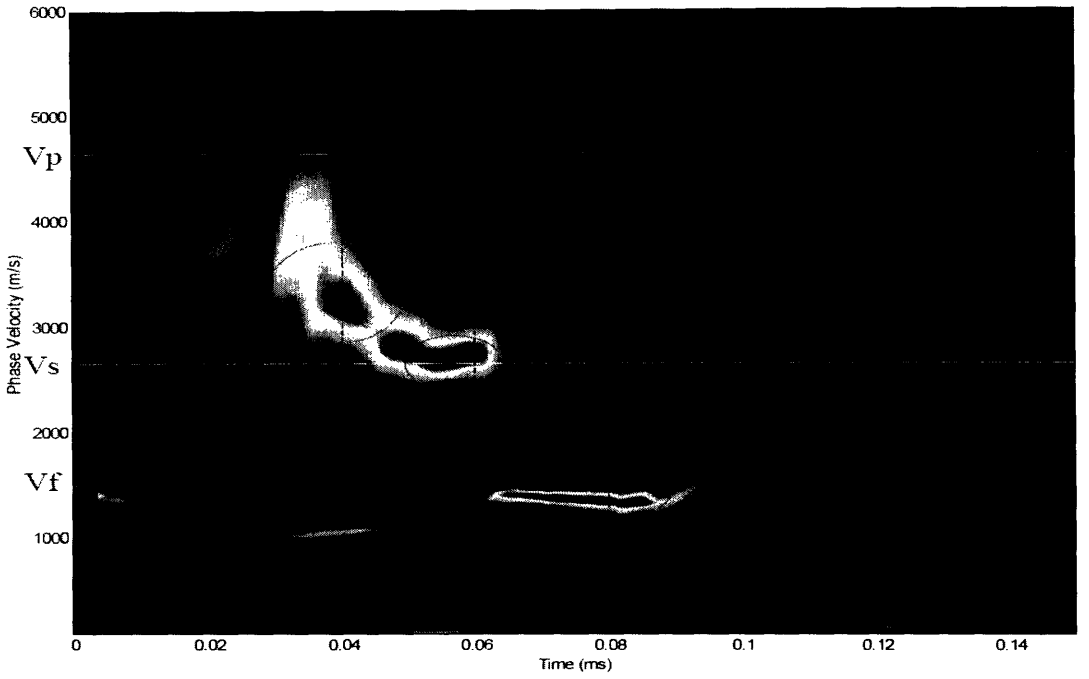

Fig 4.8 The time domain semblance of the monopole acoustic waveforms in figure 4.6. (The three circles indicates the monopole tool wave, shear wave and stonely wave respectively from top to bottom.Compressional wave is not very clear in this figure. Vp stands for the formation P wave velocity, Vs for S wave velocity, Vf for fluid wave velocity.)

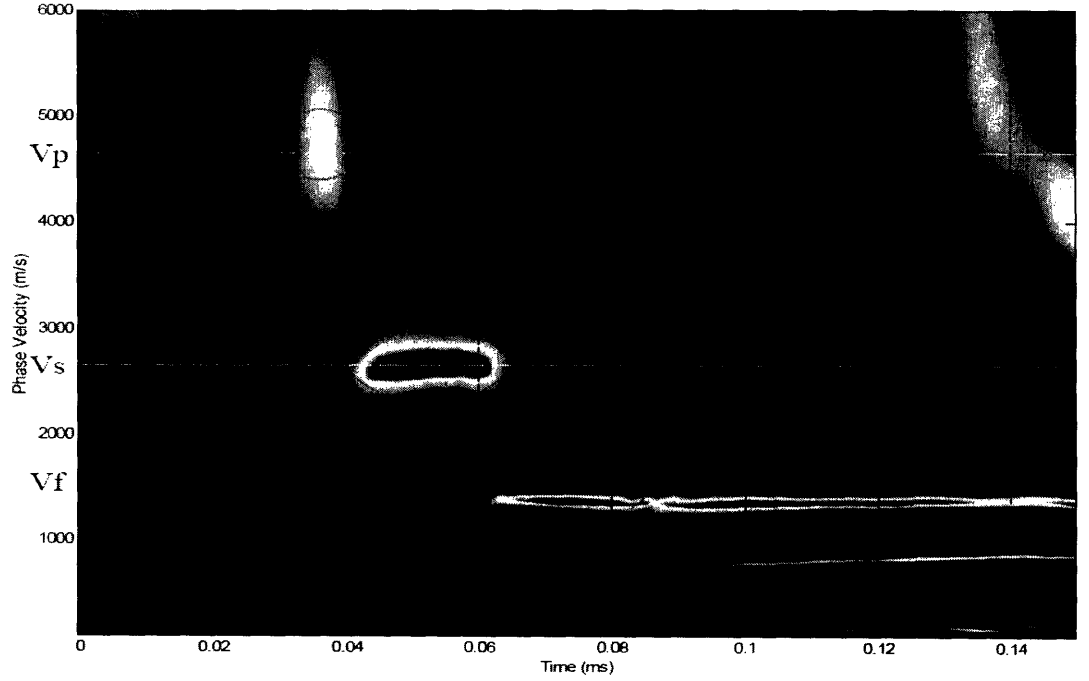

Fig 4.9 The time domain semblance of the monopole electric waveforms in figure 4.6. (The three circles indicates the monopole compressional wave, shear wave and stonely wave respectively from the top to bottom. Vp stands for the formation P wave velocity, Vs for S wave velocity, Vf for fluid wave velocity.)

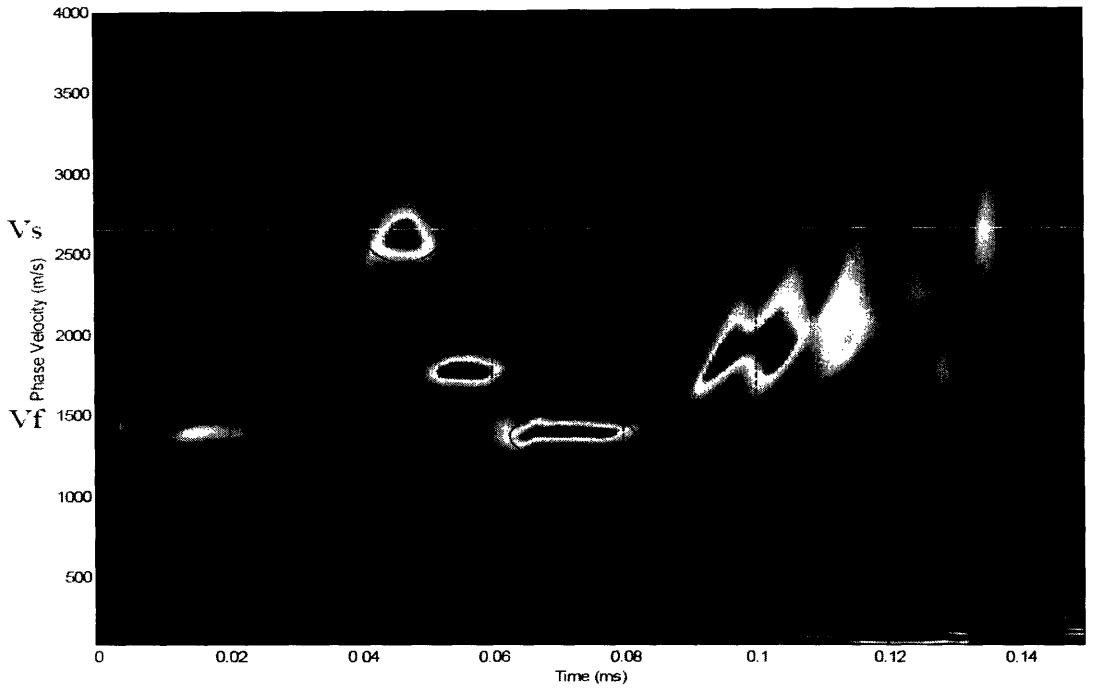

Fig 4.10 The time domain semblance of the dipole acoustic waveforms in figure 4.7. (The three circles indicates the 1st order dipole formation flexural wave, tool wave and 2nd order formation flexuraly wave respectively from the above to the bottom. Vs stands for formation S wave velocity. Vf for fluid wave velocity.)

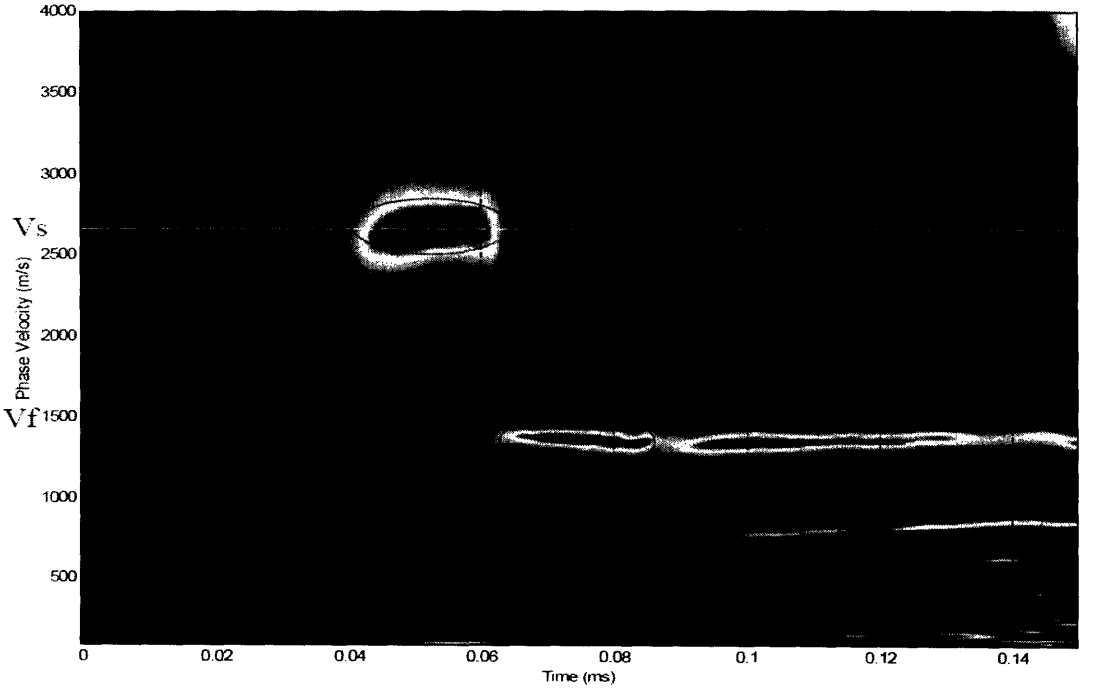

Fig 4.11 The time domain semblance of the dipole electric waveforms in figure 4.7. (The two circles indicates the 1st order dipole formation flexural wave and 2nd order formation flexuraly wave respectively from the above to the bottom. Vs stands for formation S wave velocity, Vf for fluid wave velocity.)

Chapter 5

Conclusions

In this thesis we studied the electric fields induced by borehole monopole and dipole LWD acoustic waves both experimentally and theoretically. We developed laboratory experimental set-up and procedures as well as processing methods to enhance the recorded seismoelectric signal. We also developed a Pride-theory-based model for the acoustic wave induced electric field in the LWD geometry. A suite of acoustic and seismoelectric measurements are made to demonstrate and understand the mechanism of the borehole seismoelectric phenomena, especially under LWD acoustic excitation. The numerical simulations were made for the same mechanism and borehole geometry to further support the experiment results

We measured both acoustic and seismoelectric signals under exactly the same settings in our scaled laboratory borehole . The acoustic property of the scaled experimental tool and the formation response were examined first to validate the tool's characteristics. Theoretical velocity dispersion curves were calculated and compared with the experimental data, and the effect of tool modes on the acoustic LWD signal were illustrated. We compared

experimental LWD acoustic and seismoelectric signals in both time and frequency domains. The difference between these two signals are the tool modes. We showed that the tool modes can be filtered out using a filter designed from the coherence curve of the two signals.

From both the experimental and theoretical study, the following two conclusions can be reached:

1. LWD seismoelectric signals do not contain contributions from tool modes.

2. By correlating the LWD seismoelectric and acoustic signals, we can effectively separate the real acoustic modes from the tool modes and improve the overall signal to noise ratio in acoustic LWD data.

This thesis has taken the first step towards understanding borehole LWD seismoelectric phenomena. With future improvements in both theory and instrumentation, seismoelectric LWD could evolve into a robust logging method routinely used in the not-too-distant future.

Appendix A

Layered model and boundary conditions in the LWD acoustic modeling

To model the acoustic wave propagation during logging-while-drilling (LWD), we have to take the effect of the drill collar into consideration. An acoustic logging tool can be modeled as a cylindrical structure in the borehole (Tang et al., 2002b). In total, four layers construct the LWD model of which the geometry is shown in Fig 4.1. The Thomson-Haskell propagator matrix method is used to connect the wavefield through the layers (Schmitt, 1988).

Cylindrical coordinates (r,θ,z) are used in the calculations. The radius of the inner fluid layer is r_1, tool radius is r_2, the borehole radius is r_3, and the formation is an infinite homogenous elastic formation. Both the source and receivers are located at the tool outer radius, where $r_{source} = r_{receiver} = r_2$.

The displacement potentials for each layer can be expressed as following in the axial wavenumber k - domain,

inner fluid layer: $\phi_1 = e^{ikz}\frac{1}{n!}\left(\frac{fr_0}{2}\right)^n A_1 I_n(kp_1 r)\cos(n(\theta-\phi)) \quad (K_n(r\to 0)\to\infty)$

(A.1)

$$\phi 2 = e^{ikz}\frac{1}{n!}\left(\frac{fr_0}{2}\right)^n [A_2 I_n(kp_2 r) + B_2 K_n(kp_2 r)]\cos(n(\theta-\phi))$$

rigid tool layer: $\chi_2 = e^{ikz}\frac{1}{n!}\left(\frac{fr_0}{2}\right)^n [C_2 I_n(ks_2 r) + D_2 K_n(ks_2 r)]\sin(n(\theta-\phi))$ (A.2)

$$\Gamma_2 = e^{ikz}\frac{1}{n!}\left(\frac{fr_0}{2}\right)^n [E_2 I_n(ks_2 r) + F_2 K_n(ks_2 r)]\cos(n(\theta-\phi))$$

outer fluid layer: $\phi_3 = e^{ikz}\frac{1}{n!}\left(\frac{fr_0}{2}\right)^n [A_3 I_n(kp_3 r) + B_3 K_n(kp_3 r)]\cos(n(\theta-\phi))$ (A.3)

$$\phi 2 = e^{ikz}\frac{1}{n!}\left(\frac{fr_0}{2}\right)^n B_4 K_n(kp_4 r)\cos(n(\theta-\phi))$$

formation layer: $\chi_2 = e^{ikz}\frac{1}{n!}\left(\frac{fr_0}{2}\right)^n D_4 K_n(ks_4 r)\sin(n(\theta-\phi))$ $(I_n(r\to\infty)\to\infty)$

$$\Gamma_2 = e^{ikz}\frac{1}{n!}\left(\frac{fr_0}{2}\right)^n F_4 K_n(ks_4 r)\cos(n(\theta-\phi))$$

(A.4)

where ϕ_j, χ_j and Γ_j are the compressional, vertically polarized shear wave and horizontally polarized shear wave potential of the jth layer respectively; n is the azimuthal order number with $n = 0,1,2$ corresponding to monopole, dipole and quadrupole source, respectively; I_n and $K_n(n = 0,1,\ldots)$ are the modified Bessel functions of the first and second kind of order n; ω is the angular frequency; $kp_j = \frac{\omega}{\alpha_j}$ and $ks_j = \frac{\omega}{\beta_j}$ are the compressional and shear wavenumber for the jth layer; and α_j and β_j are the compressional and shear velocity, respectively. The cylindrical coordinates (r,θ,z) are used where ϕ is a reference angle to which the point source locations are referred to. And $A_1, A_2, B_2, C_2, D_2, E_2, F_2, A_3, B_3, B_4, D_4, F_4$ are the total 12 coefficients to be

decided by the acoustic boundary conditions for the 4 layers indicated by the subscripts.

Applying the unbounded boundary conditions to the three boundaries in the LWD geometry, we can solve for the 12 unknowns in equations (A.1) to (A.4). The boundary conditions are the continuity of the radial displacement u and stress element σ_{rr}, and the vanishing of the other two shear stress elements $\sigma_{r\theta}$ and σ_{rz}. The radial fluid displacement u and stress element σ_{rr} can be expressed as

$$u = e^{ikz}\frac{1}{n!}\left(\frac{fr_0}{2}\right)^n \cos(n(\theta-\phi)\left(A_n\left[-nI_{n-1}(kr)/r + kI_n(kr)\right)I_n(kr)\right] + B_n\left[-nK_{n-1}(kr)/r - kK_n(kr)\right])$$

$$\sigma_{rr} = e^{ikz}\frac{1}{n!}\left(\frac{fr_0}{2}\right)^n \cos(n(\theta-\phi) - \rho_f\omega^2\left[A_nI_n(kr) + B_nK_n(kr)\right]$$

. (A.5)

Thus, the radial fluid displacement u_1 and u_3 and stress element σ_{rr1} and σ_{rr3} can be obtained from the above expression by involving the coefficients A_1, A_3, B_3 for the inner and outer fluid layer.

A propagator matrix is calculated to connect the wavefield in the adjacent layers. The displacement-stress vector can be defined as:

$$S = (u, v, w, \sigma_{rr}, \sigma_{r\theta}, \sigma_{rz})^T \tag{A.6}$$

where superscript T stands for transpose, and we can have

$$S = TX \tag{A.7}$$

where $X = (A_n, B_n, C_n, D_n, E_n, F_n)^T$. T is a complex 6×6 matrix whose elements can be found in Schmitt (1987). This results in

inner fluid – tool boundry: $$T_1\begin{bmatrix} A_2 \\ B_2 \\ C_2 \\ D_2 \\ E_2 \\ F_2 \end{bmatrix} = \begin{bmatrix} u_1 \\ \sigma_{rr1} \\ 0 \\ 0 \end{bmatrix} \qquad (A.8)$$

tool – outer fluid boundary: $$T_2\begin{bmatrix} A_2 \\ B_2 \\ C_2 \\ D_2 \\ E_2 \\ F_2 \end{bmatrix} + \begin{bmatrix} u_{source} \\ 0 \\ 0 \\ 0 \end{bmatrix} = \begin{bmatrix} u_2 \\ \sigma_{rr2} \\ 0 \\ 0 \end{bmatrix} \qquad (A.9)$$

outer fluid – borehole boundary: $$T_3\begin{bmatrix} 0 \\ B_4 \\ 0 \\ D_4 \\ 0 \\ F_4 \end{bmatrix} = \begin{bmatrix} u_2 \\ \sigma_{rr2} \\ 0 \\ 0 \end{bmatrix} \qquad (A.10)$$

where T_j is the propagator matrix for the jth layer. Since the acoustic ring source which is described in detail in section 4.1.1 is placed on the rigid tool rim, we have to add a source displacement term to the tool radial displacement (White et al., 1968). The expression of the source displacement u_{source} is given in equation (4.1).

Equations (A.8) through (A.10) can be combined to form a 12×12 matrix. By solving this 12×12 matrix, all 12 unknowns to describe the acoustic fields in the 4 layers for the LWD model can be determined.

Appendix B

Pride theory for the coupled electromagnetic and acoustic fields of a fluid-filled porous medium

Coupled acoustic and electromagnetic fields in a homogeneous porous formation may be described by Pride's governing equations (Pride, 1994). For a harmonic field with time dependence of $\exp(i\omega t)$, the coupling between mechanical motion and electric field is expressed as

$$J = \sigma E + L(-\nabla p + \omega^2 \rho_f u) \qquad (B.1)$$

$$-i\omega w = LE + (-\nabla p + \omega^2 \rho_f u)\kappa/\eta \qquad (B.2)$$

where J is the total electric current density, E is the electric field strength, u is the solid frame displacement, w is the fluid filtration displacement and p is the pore fluid pressure. L is the coupling coefficient, ρ_f and η are the density and the viscosity of the pore fluid, κ and σ are the dynamic permeability and conductivity of the porous medium respectively, and ω is the angular frequency. Detailed expressions of L and κ are given in Appendix C.

In the frequency domain, u, w, and E obey the following set of equations (Pride and Haartsen, 1996):

$$
\begin{aligned}
&(H-G)\nabla\nabla\cdot u + G\nabla^2 u + \omega^2\rho u + C\nabla\nabla\cdot w + \omega^2\rho_f w = 0\\
&C\nabla\nabla\cdot u + \omega^2\rho_f u + M\nabla\nabla\cdot w + \omega^2\tilde{\rho}w - i\omega\tilde{\rho}LE = 0\\
&\nabla\nabla\cdot E - \nabla^2 E - \omega^2\mu\tilde{\varepsilon}E + i\omega^3\mu\tilde{\rho}Lw = 0
\end{aligned}
\qquad (B.3)
$$

where ε is the permittivity of the formation, $\tilde{\varepsilon} = \varepsilon + i\sigma/\omega - \tilde{\rho}L^2$ is the effective electrical permittivity of the formation, ρ is the density of the formation, $\tilde{\rho} = i\eta/(\omega\cdot k)$ is the effective density for the relative flow, G is the shear modulus of the formation, and H, C, and M are porous medium moduli. The formation parameters $\rho, H, C,$ and M can be expressed as

$$
\begin{aligned}
&\rho = (1-\phi)\rho_s + \phi\rho_f,\\
&H = K_b + 4G/3 + (K_s - K_b)^2/(D - K_b),\\
&C = K_s(K_s - K_b)/(D - K_b),\\
&M = K_s^{\,2}/(D - K_b),
\end{aligned}
\qquad (B.4)
$$

where $D = K_s\left[1 + \phi(K_s/K_f - 1)\right]$, and ϕ is the formation porosity, K_s and K_f are the bulk moduli of the solid grain and the fluid and ρ_f and ρ_s are the densities of the grain and fluid.

Once u, w, and E are know, all the other quantities can be determined. The magnetic field can be determined by Faraday's law,

$$B = -i(\nabla\times E)/\omega. \qquad (B.5)$$

And the magnetic field strength H can be obtained by

$$H = B/\mu \qquad (B.6)$$

where μ is the magnetic permeability of the formation.

Appendix C

Expressions for the coupling coefficient L and dynamic permeability κ

The dynamic permeability κ and the electrokinetic coupling coefficient L that appear in equations $(B.1)$ and $(B.2)$ are very important to the electrokinetic phenomena. Both are frequency dependent. When L goes to zero, Pride's equation separates to Maxwell's equations for an electromagnetic field, and Biot's equations (Biot, 1962) for a mechanical field in porous media. The expressions for L and κ are as follows

$$\frac{\kappa(\omega)}{\kappa_0} = \left[\left[1 - i\frac{\omega}{\omega_c}\frac{4}{m}\right]^{\frac{1}{2}} - i\frac{\omega}{\omega_c}\right]^{-1}$$
$$\frac{L(\omega)}{L_0} = \left[1 - i\frac{\omega}{\omega_c}\frac{m}{4}(1 - 2\frac{\tilde{d}^2}{\Lambda})(1 - i^{\frac{3}{2}}\frac{\tilde{d}}{\delta})^2\right]^{-\frac{1}{2}} \qquad (C.1)$$

where κ_0 is the Darcy permeability, $\omega_c = \varphi\eta/\alpha_\infty\kappa_0\rho_f$ is the transition frequency from viscous flow to inertial flow, α_∞ is tortuosity, m is a dimensionless parameter defined as $m = \phi\Lambda^2/\alpha_\infty\kappa_0$ and is assumed to be 8 in our calculation, Λ is the characteristic pore size, $\delta = \sqrt{\eta/\omega\rho_f}$ is the viscous skin depth, $\tilde{d}$ is less than or equal to the Debye length d,

$$\tilde{d} \le d = \sqrt{\varepsilon_f k_B T / e^2 z^2 N} \qquad (C.2)$$

where ε_f is the fluid permittivity, k_B is the Boltzman constant, T is absolute temperature, e is the electric charge, z is the ionic valence of the solution, and N is ion concentration and defined as $N = 6.022 \times 10^{26} \times molarity$.

L_0 is the low frequency limit of the coupling coefficient which can be determined by experiments as done by Li et al. (1995) and expressed as

$$L_0 = -\frac{\phi}{\alpha_\infty}\frac{\varepsilon_f \varsigma}{\eta}\left[1 - a\alpha_\infty \frac{\tilde{d}}{\Lambda}\right] \qquad (C.3)$$

where ς is the zeta potential on the slipping plane and a is a constant assumed to be 2 in my calculation.

Pride and Morgan (1991) find an expression for ς based on experiments as follows,

$$\varsigma = 0.008 + 0.026 \log_{10}(C) \qquad (C.4)$$

where C is the molarity of the solution.

The porous medium properties used in my calculation are given in table C.1 where ε_0 is the permittivity in the vacuum.

	Porosity (%)	Ks (GPa)	Solid density (kg/m^3)	Solid Vp (m/s)	Solid Vs (m/s)	Permeability (darcy)
Slow formation	20	35	2600	2000	1200	1
Pore fluid density = 1000 (kg/m^3)			Pore fluid viscosity =0.001 Pa .S			
Pore fluid permittivity = $80\varepsilon_0$			Formation permittivity = $4\varepsilon_0$			

Table C.1 Medium properties used in the calculation of the coupling coefficient L

Bibliography

Aki, K. and Richards, P. G. (1980). *Quantitative Seismology, Theory and Methods.* W. H. Freeman and Co., San Francisco.

Aron, J., Chang, S., Dworak, R., Hsu, K., Lau, T., Mas
son, J., Mayes, J., McDaniel, G., Randall, C., Kostek, S., and Plona, T. (1994). Sonic compressional measurements while drilling. *SPWLA 35th Annual Logging Symposium.*

Biot, M. A. (1941). General theory of three-dimensional consolidation. *J. Applied Phys.,* 12, 155-164.

Biot, M. A. (1956a). Theory of propagation of elastic waves in a fluid-saturated porous solid. I. Low-frequency range. *J. Acoust. Soc. Am.,* 28, 168-178.

Biot, M. A. (1956b). Theory of propagation of elastic waves in a fluid-saturated porous solid. II. High-frequency range. *J. Acoust. Soc. Am.,* 28, 179-191.

Biot, M. A. (1962). Mechanics of deformation and acoustic propagation in porous media. *J. Applied Phys.,* 33, 1482-1489.

Biot, M. A. (1952). Propagation of elastic waves in a cylindrical bore containing a fluid. *J. Appl. Phys.,* 23, 997-1005.

Bockris, J. and Reddy, A. K. N. (2000). *Modern electrochemistry.* Plenum Press, New York.

Bouchon, M. and Schimitt, D. (1989). Full-wave acoustic logging in an irregular borehole. *Geophysics*, 54, 758-765.

Bouchon, M. (2003). A review of the discrete wavenumber method. *Pure and Applied Geophysics.* 160, 445-465.

Butler, K. E. and Russell, R. D. (1993). Subtraction of powerline harmonics from geophysical records. *Geophysics*, 58, 889-903.

Butler, K. E. and Russell, R. D. (2003). Cancellation of multiple harmonic noise series in geophysical records. *Geophysics*, 68, 1083-1090.

Chen, S. T. and Eriksen, E. A. (1991). Compressional and shear-wave logging in open and cased holes using a multipole tool. *Geophysics,* 61, 437-443.

Cheng, C. H. and Toksöz, M. N. (1981). Elastic wave propagation in a fluid-filled borehole and synthetic acoustic logs. *Geophysics,* 46, 1042-1053.

Cheng, N. Y. and Cheng, C. H. (1996). Estimation of formation velocity, permeability, and shear-wave anisotropy using acoustic logs. *Geophysics,* 56, 550-557.

Chi, S. H, Toksöz, M. N., and Xin, Z. (2005). Theoretical and numerical studies of seismoelectric conversions in boreholes. *Submitted to Proceeding of the 17th International Symposium of Nonlinear Acoustics, Pennsylvania State University. Published by American Institute of Physics.*

Chi, S. H., Zhu, Z., Rao, V. N. R., and Toksöz, M. N. (2005). Higher order modes in acoustic logging while drilling. *Borehole Acoustic and Logging / Reservoir Delineation Consortia Annual Report, MIT.*

Cittá, F., Russell, C., Deady, R., and Hinz D. (2004). Deepwater hazard avoidance in a large top-hole section using LWD acoustic data. *The Leading Edge*, 23, 566-573.

Desbrandes, R. (1985). *Encyclopedia of well logging.* Gulf Publishing Company.

Dukhin, S. S. and Derjaguin, B. V. (1974). Electrokinetic phenomena. John Wiley and Sons, Inc.

Esmersoy, C., Hawthorn A., Durrand, C., and Armstrong P. (2005). Seismic MWD: Drilling in time, on time, it's about time. *The Leading Edge*, 24, 56-62.

Fitterman, D. V. (1979). Relationship of the self-potential Green's function to solutions of controlled source direct-current potential problems. *Geophysics,* 44, 1879-1881.

Haartsen, M. W. (1995). *Coupled electromagnetic and acoustic wavefield modeling in poro-elastic media and its applications in geophysical exploration.* Ph.D. thesis, Massachusetts Institute of Technology, Department of Earth, Atmospheric and Planetary Sciences.

Haartsen, M. W., Zhu, Z., and Toksöz, M. N. (1995). Seismoelectric experimental data and modeling in porous layer models at ultrasonic frequencies. In *Expanded Abstract, 65th Ann. Internat. Mtg.*, pages 26-29. Soc. Expl. Geophys.

Haartsen, M. W. and Pride, S. R. (1997). Electroseismic waves from point source in layered media. *J. Geophys Res.,* 102, 24745-24769.

Hsu, C. J., Kostek, S., and Johnson, D. L. (1997). Tube waves and mandrel modes: experiment and theory. *J. Acoust. Soc. Am.,* 102, 3277-3289.

Hu, H. S., Wang, K. X., and Wang, J. N. (2000). Simulation of an acoustically induced electromagnetic field in a borehole embedded in a porous formation. *Borehole Acoustic and Logging / Reservoir Delineation Consortia Annual Report, MIT.*

Hu, H. S. and Liu, J. Q. (2002). Simulation of the converted electric field during acoustoelectric logging. *SEG Int'l Exposition and 72nd Annual Meeting, Salt Lake City, Utah, 2002, October 6-11.*

Huang, X. (2003). *Effects of tool positions on borehole acoustic measurement: a stretched grid finite difference approach.* Ph.D. thesis, Massachusetts Institute of Technology, Department of Earth, Atmospheric and Planetary Sciences.

Hunter, Robert J. (2001). *Foundations of colloid science.* Oxford University Press, New York

Ishido, T. and Mizutani, H. (1981). Experimental and theoretical basis of electrokinetic phenomena in rock-water systems and its applications to geophysics. *J. Geophys Res.,* 86, 1763-1775.

Ivanov, A. G. (1940). The electroseismic effect of the second kind. *Izvestiya Akademii Nauk SSSR, Ser. Geogr. Geofiz.*, 5, 699-727.

Joyce, B., Patterson, D., Leggett, J. V., and Dubinsky, V. (2001). Introduction of a new omni-directional acoustic system for improved real-time LWD sonic logging-tool design and field test results. *SPWLA 42nd Annual Logging Symposium.*

Kimball, C. V., and Marzetta, T. L. (1984). Semblence processing of borehole acoustic array data. *Geophysics*, 49, 274-281.

Kurkjian, A. L. and Chang, S. K. (1986). Acoustic multipole sources in fluid-filled boreholes. *Geophysics*, 51, 148-163.

Li, S. X., Pengra, D. B., and Wang, P. Z. (1995). Onsagers reciprocal relation and the hydraulic permeability of porous media. *Phys. Rev. E,* 51, 5748-5751.

Loren, B., Perrier, F., and Avouac, J. P. (1999). Streaming potential measurements 1. Properties of the electrical double layer from crusted rock samples. *J. Geophys Res.,* 104, 17857-17877.

Market, J., Althoff, G., Barnett, C., and Deady, R. (2002). Processing and quality control of lwd dipole sonic measurements. *SPWLA 43rd Annual Logging Symposium, Osio, Japan.*

Markov, M. G. and Verzhbitskiy, V. V. (2004). Simulation of the electroseismic effect produced by an acoustic multipole source in a fluid-filled borehole. *SPWLA 43rd Annual Logging Symposium, 2004, June 6-9,* paper VV.

Minear, J., Birchak, R., Robbins, C., Linyaev, E., and Mackie, B. (1995). Compressional wave slowness measurement while drilling. *SPWLA 36th Annual Logging Symposium.*

Mikhailov, O. V. (1998). *Borehole electroseismic phenomena.* Ph.D. thesis, Massachusetts Institute of Technology, Department of Earth, Atmospheric and Planetary Sciences.

Mikhailov, O. V., Queen, J., and Toksöz, M. N. (2000). Using borehole electroseismic measurements to detect and characterize fractured (permeable) zones. *Geophysics*, 65, 1098-1112.

Nolte B., Rao, V. N. R., and Huang, X. (1997). Dispersion analysis of split flexural waves. *Borehole Acoustic and Logging / Reservoir Delineation Consortia Annual Report, MIT.*

Peterson, E. W. (1974). Acoustic wave propagation along a fluid-filled cylinder. *J. Appl. Phys.,* 45, 3340-3350.

Pride, S. R. and Morgan, R. D. (1991). Electrokinetic dissipation induced by seismic waves. *Geophysics*, 56, 914-925.

Pride, S. R. (1994). Governing equations for the coupled electromagnetics and acoustics of porous media. *Phys. Rev. B*, 50, 15678-15696.

Pride, S. R. and Haartsen, M. W. (1996). Electroseismic wave properties. *J. Acoust. Soc. Am.,* 100, 1301-1315.

Rao, V. N. R., Burns, D. R., and Toksöz, M. N. (1999). Models in LWD applications. *Borehole Acoustic and Logging / Reservoir Delineation Consortia Annual Report, MIT.*

Rao, V. N. R. and Toksöz, M. N. (2005). Dispersive wave analysis – method and applicatoins. *Borehole Acoustic and Logging / Reservoir Delineation Consortia Annual Report, MIT.*

Reppert, P. M., Morgan, F. D., Lesmes, D. P., and Jouniaux, L. (2001). Frequency-dependent streaming potentials. *Journal of Colloid and Interface Science,* 234, 194-203.

Rover, W., Rosenbaum, J., and Ving, T. (1974). Acoustic waves from an impulsive source in a fluide-filled borehole. *J. Acoust. Soc. Am.,* 55, 1144-1157.

Russell, R. D., Butler, K. E., Kepic, A. W., and Maxwell, M. (1997). Seismoelectric exploration. *The Leading Edge*, 16, 1611-1615.

Schimitt, D. P. (1986). Full wave synthetic acoustic logs in saturated porous media. Part I. A review of Biot's theory . *ERL Full Waveform Acoustic Logging Consortium Annual Report,* 1986, 105-153.

Schimitt, D. P. (1986). Full wave synthetic acoustic logs in saturated porous media. Part II. Simple configuration . *ERL Full Waveform Acoustic Logging Consortium Annual Report,* 1986, 175-208..

Schimitt, D. P. and Cheng, C. H. (1987). Shear wave logging in (multilayered) elastic formations: an overview. *ERL Full Waveform Acoustic Logging Consortium Annual Report,* 1987, 213-237.

Schimitt, D. P. (1988). Transversely isotropic saturated porous formations: I. Theoretical developments and (quasi) body wave properties. *ERL Full Waveform Acoustic Logging Consortium Annual Report,* 1988, 247-290.

Schimitt, D. P. (1989). Acoustic multipole logging in transversely isotropic poroelastic formations. *J. Acoust. Soc. Am.,* 86, 2397-2421.

Segesman, F. (1962). New SP correction charts. *Geophysics,* 27, 815-828.

Segesman, F. F. (1980). Well-logging method. *Geophysics,* 45, 1667-1684.

Sill, W. R. (1983). Self-potential modeling from primary flows. *Geophysics,* 48, 76-86.

Sprunt, E. S., Mercer, T. B., and Djabbarah, N. F. (1994). *Geophysics,* 59, 707-711.

Tang, X. M. and Cheng, C. H. (1993). Effects of a logging tool on the Stoneley waves in elastic and porous boreholes. *Log Analyst*, 34, 46-56.

Tang, X. M., Wang, T., and Patterson, D. (2002). Multipole acoustic logging-while-drilling. *SEG Technical Program and Expanded Abstract,* 2002, 364-367

Tang, X. M., Dubinsky, V., Wang, T., Bolshakov, A., and Patterson, D. (2002). Shear-velocity measurement in the logging-while-drilling environment: modeling and field evaluations. *SPWLA 43rd Annual Logging Symposium, 2002, June 2-5,* paper RR..

Tang, X. M. and Cheng, C. H. (2004). *Quantitative borehole acoustic methods*. Elsevier, Science Publishing Co., Oxford.

Thompson, A. and Gist, G. (1993). Geophysical applications of electrokinetic conversion. *The Leading Edge*, 12, 1169-1173.

Tsang, L. and Rader, D. (1979). Numerical evaluation of transient acoustic waveforms due to a point source in a fluid-filled borehole. *Geophysics*, 44, 1706-1720.

White, J. E. and Zechman, R. E. (1968). Computed response of an acoustic logging tool. *Geophysics,* 33, 302-310.

White, J. E. (1983). *Underground sound.* Elsevier, Science Publishing Co., Amsterdam.

Zhu, Z. and Toksöz, M. N. (1996). Experimental studies of electrokinetic conversion in fluid-saturated porous medium. In *Expanded Abstracts, 66th Ann. Internat. Mtg.*, pages 1699-1702. Soc. Expl. Geophys.

Zhu, Z. and Toksöz, M. N. (1997). Experimental studies of electrokinetic conversion in fluid-saturated borehole models. In *Expanded Abstracst, 67th Ann. Internat. Mtg.*, pages 334-337. Soc. Expl. Geophys.

Zhu, Z. and Toksöz, M. N. (1998). Seismoelectric and seismomagnetic measurements in fractured borehole models. In *Expanded Abstract, 69th Ann. Internat. Mtg.*, pages 144-147. Soc. Expl. Geophys.

Zhu, Z., Haartsen, M. W., and Toksöz, M. N. (1999). Experimental studies of electrokinetic conversions in fluid-saturated borehole models. *Geophysics*, 64, 1349-1356.

Zhu, Z., Haartsen, M. W., and Toksöz, M. N. (2000). Experimental studies of electrokinetic conversions in fluid-saturated porous media. *J. Geophys Res.,* 105, 28055-28064.

Zhu, Z. and Toksöz, M. N. (2003). Crosshole seismoelectric measurements in borehole models with fractures. *Geophysics*, 68, 1519-1524.

Zhu, Z., Rao, V. N. R., and Burns, D. R., and Toksöz, M. N. (2004). Experimental studies of multipole logging with scaled borehole models. *Borehole Acoustic and Logging / Reservoir Delineation Consortia Annual Report, MIT.*

Zhu, Z., Chi, S. H., and Toksöz, M. N. (2005). Experimental and theoretical studies of seismoelectric effects in boreholes. *Borehole Acoustic and Logging / Reservoir Delineation Consortia Annual Report, MIT.*